1-2021

Identification of Ice-rafted Debris in the Weddell Sea to Characterize Glaciation at the Eocene-Oligocene Transition

Josie Horowitz
Montclair State University

ABSTRACT

At the Eocene-Oligocene transition (EOT), approximately 34 million years ago (Ma), the Earth's climate changed from a warm greenhouse to a cooler climate which resulted in ice-sheet growth and stable continental-scale ice sheets in Antarctica. Hole 696B of the Ocean Drilling Program Leg 113 drilled in 650 m of water depth on the South Orkney Microcontinent spans the entire EOT. Cores 53R and 54R are dated at lower Oligocene (~33.1 to ~33.5 Ma) and total ~14 meters in thickness from ~549 to ~564 mbsf. Ice-rafted debris (IRD) in sediment cores gives insight into the extent of glaciation in West Antarctica, as well as the evolution of deep-sea cooling during the EOT. Distinguishing between sea-ice rafted debris (SIRD) and iceberg rafted debris (IBRD) provides information about weathering processes and depositional environments.

Laser Particle Size Analysis was used to determine the volume percentage of sediment in different size classes, i.e. the grain size distribution of 113 samples. IRD was identified by examining quartz grains >150 μm. Samples with large volume percentages of coarse grains were sieved to obtain the sand fraction of grains >150 μm. 5 samples with the greatest yield of grains >150 μm were selected for microtexture analysis using the Scanning Electron Microscope (SEM). SEM with Energy Dispersive Spectroscopy (EDS) was used to identify quartz grains. SIRD and IBRD grains were distinguished by examining physical topography and microtextures in Secondary Electron images.

Quartz grains were categorized into 7 groups based on roundness, grain relief, amount of silica dissolution, and presence of grain fractures. The 7 types are further grouped by IRD type where IBRD types have little to no silica dissolution, angular/sub-angular grains, with fractures present; SIRD types have silica dissolution, rounded/sub-rounded grains, with little to no fractures present. 185 grains from 5 samples were analyzed using EDS and SEM, 105 of which were quartz

grains. Based on the grain type groupings, 35% of the quartz grains are IBRD and 60% are SIRD, and 5% is not glacially influenced, and therefore, not an IRD type of grain. The ratio of SIRD to IBRD is uniform in sample 3. SIRD grain types are dominant in the rest of samples 1, 2, 4, and 5. This research concludes that IRD is present in the early Oligocene 33.48 Ma and supports that ice sheets were present in West Antarctica with widespread cooling and extensive glaciation during this time.

MONTCLAIR STATE UNIVERSITY

Identification of Ice-rafted Debris in the Weddell Sea to Characterize Glaciation at the Eocene-Oligocene Transition

by

Josie Horowitz

A Master's Thesis Submitted to the Faculty of

Montclair State University

In Partial Fulfillment of the Requirements

For the Degree of

Master of Science

January 2021

College of Science and Mathematics

Department of Earth and
Environmental Studies

Thesis Committee:

[redacted]

Dr. Sandra Passchier
Thesis Sponsor

[redacted]

Dr. Ying Cui
Committee Member

[redacted]

Dr. Josh Galster
Committee Member

Identification of ice-rafted debris in the Weddell Sea to characterize glaciation at the Eocene-Oligocene transition

A THESIS

Submitted in partial fulfillment of the requirements
for the degree of Master of Science

by

Josie Horowitz

Montclair State University

Montclair, New Jersey

2021

ACKNOWLEDGEMENTS

First and foremost, to my thesis sponsor, Dr. Sandra Passchier. Because of you, I was able to achieve what I came to MSU for. Beyond that, you provided a safe and positive environment, where I was able to make mistakes and learn without feeling discouraged. Despite some setbacks, you were always available and optimistic. This would not have been possible without your advice, dedication, and interest in my success. Lastly, you gave me the opportunity to do research at IODP at Texas A&M University, which was an unforgettable experience and I hope to visit again. Material and salary support for this project is from the National Science Foundation award # ANT 1743643

To Dr. Ying Cui and Dr. Josh Galster, for agreeing to be on my committee and taking the time from busy schedules to review my thesis, provide comments, and listen to my defense. Dr. Ying Cui, you pose challenging questions that push students to think, and your patience while we ponder is valued. Dr. Josh Galster, while you may have a different area of expertise, you provided input from a different perspective which is always appreciated. To Dr. Passchier's lab group – Victoria Hojnacki and Olga Libman-Roshal, not only did we discuss literature to great lengths and work on projects in our many classes together, but I sincerely enjoyed your company. I hope there is opportunity for our us to work together in the future.

Thank you to my family for continued support throughout my college education. Lastly, thank you to Jay for pushing me even when I thought I could not succeed. I would not have had the courage to go back for my master's degree without your constant support. Thank you for enduring all those late nights with me while I crammed for tests, whined about homework, and dealt with computer issues. And lastly, for never letting me give up.

TABLE OF CONTENTS

LIST OF FIGURES

LIST OF TABLES

1. INTRODUCTION

1.1 Background

1.1.1 Importance of Research

The West Antarctic Ice Sheet (WAIS) is losing ice at a rate of 4.5 cm sea level equivalent per century (Holland et al., 2019) and the average annual temperature of the WAIS has increased approximately 2.4ºC since 1958 (Bromwich et al., 2013). Moreover, as global warming continues and ice sheets are melting, Antarctica has the potential to contribute 15 meters of sea level rise over the next few centuries (Whitehouse et al., 2019). Better understanding the processes that drive glaciation at the Eocene-Oligocene Transition (EOT), can help us find solutions for our present-day warming climate. If we can reconstruct ice sheet growth of West Antarctica, we can develop models to better understand current ice sheet dynamics to allow for more accurate future projections. Specifically, during a time of unpredictable climates due to rapid global warming, this will allow scientists, policy makers, environmentalists, and all of humankind to understand the immediate effects of a melting ice sheet so that we can take action and develop solutions to delay or reverse our warming climate.

1.1.2 The Eocene-Oligocene Transition in climate proxy records

The Eocene-Oligocene Transition (EOT) occurred approximately 33.7 million years ago (Ma) (Katz et al., 2008) when the Earth's climate changed from a warm greenhouse to a cooler climate. This climatic shift caused the onset of glaciation on the continent of Antarctica which occurred rapidly after a 17 million-year (m.y.) period of cooling from the early Eocene to the early Oligocene with a 3.0‰ increase in oxygen

isotopes ($\delta^{18}O$). Prior to the EOT, oscillations in global temperatures resulted in unstable ice-sheet growth and decay. Further evidence of temperature variation is expressed in geochemical proxies and fossil evidence. Approximately 18 m.y. before the EOT, a noticeable warming period marked by a peak known as the early Eocene Climatic Optimum (EECO) occurred from 52 to 50 Ma (Zachos et al., 2001).

The global cooling period of the EOT resulted in rapid ice-sheet growth in Antarctica, which remained stable at a mass approximately 50% of modern-day ice sheets until the late Oligocene at 26 Ma. This is seen in the relatively high $\delta^{18}O$ values of >2.5 ‰ (Zachos et al., 2001). Furthermore, deep sea temperatures declined from approximately 12˚C to 4.5˚C across the EOT evidenced by increasing $\delta^{18}O$ values (Figure 1) in data obtained from Veizer and Prokoph (2015). Deep sea temperatures reached approximately 4˚C by the early Oligocene with an overall continuation of low global ice volume and warmer deep-sea temperatures in the middle Miocene Climatic Optimum (MMCO) at approximately 15 Ma. Subsequently, a stable ice sheet in Antarctica coupled with gradual global cooling occurred at approximately 10 Ma.

There are two main approaches to understanding the cause of the EOT cooling and development of stable continental-scale ice sheets in Antarctica. The first notion describes the ability to transport warm atmospheric and oceanic heat away from Antarctica as the result of the opening of ocean passageways and changes in ocean circulation due to tectonics (Livermore et al., 2005). The second notion is attributable to orbital configurations during a decrease in atmospheric carbon dioxide which triggered ice-sheet growth (Zachos et al., 2001). Across the Eocene-Oligocene boundary, there was cooling at both high and low latitudes by approximately 4 to 5˚C (Coxall and Wilson, 2011).

Additionally, the calcite compensation depth (CCD), the depth at which the input of calcium carbonate ($CaCO_3$) into the ocean equals the rate of dissolution, fluctuates due to variations in ocean acidity, atmospheric carbon dioxide, and the marine carbon cycle. Geological records preserve changes in the CCD based on the weight percentage of $CaCO_3$ displaying variations in the carbon cycle (Pälike et al., 2012). Therefore, we can see that the effects on the global carbon cycle are apparent in climatic changes.

1.1.3 Development of Ice Sheets in the Southern Hemisphere

The research performed to understand the role global climate dynamics play in the formation of ice sheets at the poles is extensive in the 21st century (e.g., Coxall and Wilson, 2011; Katz et al., 2008; Zachos et al., 2001). However, estimations of the timing of the onset of glaciation in West Antarctica differ significantly. Based on analyses of $\delta^{18}O$ and $\delta^{13}C$ of benthic foraminifera, on a temporal resolution of up to 2 kyr, the first large, stable ice sheets of > 25 million km^3 in Antarctica transpired during the early Oligocene (Coxall et al., 2005; Katz et al., 2008). This occurred in a stepwise progression simultaneous with the deepening of the CCD recorded in two phases of approximately 40 kyr each and with approximately 200 kyr in between steps (Coxall et al., 2005). The first phase ensued when orbital configurations enabled cooler summers in the southern hemisphere, specifically low eccentricity, low obliquity, and consequently, diminished seasonality. Furthermore, these conditions favoring cooler summers allowed for snow to remain. This triggered ice-sheet growth accompanied by 30 m in sea level fall, 2.5^{o}C cooling, and a $\delta^{18}O$ increase of 0.9‰ at approximately 33.8 Ma, EOT-1 (‘Eocene-Oligocene Transition event 1’) (Figure 1). The second phase followed with sea level fall of 105 m, 2^{o}C cooling, and a $\delta^{18}O$ increase of 1.0‰ at 33.545 Ma, Oi-1 (‘Oligocene isotope event 1’) (Figure 1) (Katz et al., 2008)

coupled with cooling and stable, continental-scale ice sheets in Antarctica (Coxall et al., 2005).

Antarctica's paleotopography was modeled in Wilson et al. (2013) to reconstruct the growth of ice sheets at the EOT and considered thermal subsidence and elevations. Results from the model show formation of the WAIS at 33.8-33.5 Ma alongside expansion of the East Antarctic Ice Sheet and it was suggested that there was considerable glaciation in the inner continent prior to the EOT. In addition, the model determined deep-sea cooling of only 1-2^{o}C based on established interior continental ice sheets approximately 7 million km^3 in size (Wilson et al., 2013). In addition, Carter et al. (2017) analyzed provenance and microtextures of sediments from the South Orkney Microcontinent (SOM) in the Ocean Drilling Program (ODP) Leg 113 Site 696 (Cores 51R, 52R, 56R, 57R, and 59R-62R) to infer the extent of glaciation. Their results provide an indication of provenance consistent with widespread glacial calving in the Weddell Sea prior to Oi-1, which suggests extensive ice-sheet growth approximately 2.5 m.y. prior to what is typically considered the onset of glaciation at 34-35.5 Ma (Carter et al., 2017).

Conversely, Passchier et al. (2017) analyzed major-element geochemistry of bulk samples to acquire the chemical index of alteration (CIA) and the S index, the molar ratio of Na_2O and K_2O to Al_2O_3 (Passchier et al., 2017), for sediments from ODP holes 739C, 742A, and 1166A. This provided evidence of a stepwise growth of Antarctic ice sheets where mountain glaciation occurred in the late Eocene at 35.8-34.8 Ma accompanied by brief warming periods. Subsequently at 34.4 Ma, continental ice sheets advanced into Pyrdz Bay with maximum glaciation at the time of Oi-1 based on a decrease in chemical weathering intensity and cooling temperatures (Passchier et al., 2017). Based on the

differing results and interpretations from previous studies, further research with multiple methods is imperative to reconstruct the extent of glaciation prior to and during the EOT.

1.2 Study Location

1.2.1 Ocean Drilling Program Leg 113

The JOIDES Resolution vessel is used to obtain samples from the Earth that can be used to understand its geologic history as well past climate change and how we can predict climate changes in the future. The Ocean Drilling Program (ODP) led Leg 113 to the Weddell Sea using the JOIDES Resolution vessel in 1987. One objective of Leg 113 was to better understand the processes involving the formation of Antarctica's ice sheets and how the magnitude of glaciation has changed over the last 37 million years ("Ocean Drilling Program Final Technical Report," 1983-2007). The vessel recovered approximately 1,952 meters of sediment core in 22 holes of Leg 113. Approximately 215 meters of sediment core were recovered in Holes 696A and 696B at Site 696 located in Figure 2. The depth of the oldest sediment core is 645.6 meters below sea floor (mbsf). The EOT identified in Hole 696B spans lithological Unit VII at a depth of 548 mbsf to the base at 645.6 mbsf. Unit VII is divided into four subunits, with 53R and 54R residing in Subunit VIIB (548.9 – 579.4 mbsf) (Barker et al., 1988).

1.2.2 Tectonics of the Weddell Sea

The continent of Antarctica is divided into two fundamental geological units, which are separated by the Transantarctic Mountains (TAM). East Antarctica is a continental shield made of igneous and metamorphic rocks dated at >1 billion years old (Ga) with an overlying layer of younger, sedimentary rocks. Exposed bedrock of the East Antarctica

Craton is Precambrian at older than 540 Ma (Artemieva and Thybo, 2020). The geologically intricate West Antarctica we see today is the result of the subduction of oceanic crust beneath what was the supercontinent Gondwana due to back-arc extension within the Weddell Sea rift system. West Antarctica can be separated into three broad regions, each with unique geological systems. This includes: (1) the Ross Embayment, and West Antarctic rift system (WARS), and Marie Byrd Land dome; (2) the Antarctic Peninsula and the Thurston Island Crustal Block; and lastly, (3) the Weddell Sea region comprised of the Ellsworth-Whitmore Mountains, Haag Nunataks, and the shallow marine Weddell Sea rift system (Jordan et al., 2020). Additionally, the SOM currently lies in the northwest Weddell Sea sector. In the early to middle Oligocene, approximately 35-30 Ma, the SOM separated from the northern Antarctic Peninsula. This was followed by the formation of surrounding basins: the western Powell Basin and the eastern Jane Basin (Barker et al., 1984).

The Weddell Sea region, as described above, is the oldest part of West Antarctica. This region, as well as the Antarctic Peninsula, is also poorly understood in terms of climate change through the stratigraphic record. Continuous, intact sedimentary sequences are lacking, specifically during the late Eocene and younger. Therefore, it has been difficult to obtain an undisturbed archive of cooling during the EOT (Anderson et al., 2011). Despite the breakup of Gondwana during the beginning of the Jurassic period, the Weddell Sea region was minimally impacted except for its migration to where it currently resides. The Precambrian Era is observable in the oldest exposed rocks in Antarctica. Haag Nunataks formed as a result of a magmatic arc approximately 1.17 Ga and deformed 110 m.y. later. The visible outcrop displays juvenile rocks that formed directly from the mantle. There is

no evidence of deformation following the Grenville orogeny, where the Haag Nunataks took the form of a microcontinental block (Jordan et al., 2020).

Based on Hafnium isotopic signatures from detrital zircons from Jurassic granites (Flowerdew et al., 2007), the Ellsworth-Whitmore Mountains basement geology is approximately the same age as the Haag Nunataks. Prior to the breakup of Gondwana, it is thought that the Ellsworth-Whitmore Mountains, north of its current location, were receiving sediment from the supercontinent. Additionally, there is an indication of glacial sediments being transported to the Ellsworth-Whitmore Mountains from the Transantarctic Mountains through ice streams from East Antarctica in the Paleozoic era. Subsequently, the Weddell Sea region underwent continental break-up and magmatism due to the formation of large igneous provinces in the Early Jurassic. Evidence of continental movement and subduction can be seen in four granites residing in the Ellsworth-Whitmore Mountains that contain back-arc and continental rifting signatures. As continental movement in the Ellsworth-Whitmore Mountains and Haag Nunataks was occurring, the southern Weddell Sea rift system was experiencing back-arc extension of the continental crust. Oceanic magnetic anomalies show that tectonic movements had ceased in the Weddell Sea region by the end of the Jurassic period (Jordan et al., 2020). It is evident that the geologic processes associated with the formation of West Antarctica are intricate. Therefore, insight into the complexities of continental development is necessary to understanding ice sheet evolution, as well as providing key information for provenance of Core 53R and 54R in future studies.

1.3 Cores Analyzed

1.3.1 Age Model

It is common for siliceous diatom assemblages to be used in reconstructing the age of ice sheets of Antarctica. However, the preservation of diatoms in the Antarctic margin during the Eocene-Oligocene interval is poor. Until Houben et al. (2013), the precise age of Unit VII was difficult to discern due to partial core recovery on the ship (Carter et al., 2017) and poorly preserved microfossils across the EOT (Houben et al., 2013). The Eocene encompasses a multitude of dinocyst species in great abundance, prior to glaciation in Antarctica. Houben et al. (2013) utilized dinocyst stratigraphy to determine age of sediments across the Eocene-Oligocene boundary. Specifically, the First Occurrence (FO) of dinocyst species *Chriopteridium galea* in Section 53R-3 at 552.2 mbsf dated at the lower Oligocene 33.2 Ma and was used to extrapolate the age of Cores 53R and 54R (López-Quirós et al., 2019). The equation specified in the aforementioned study defines Equation (1) for Section 53R-3 where *x* is depth (mbsf) and *y* is age (Ma). Equation (1) was inverted to obtain Equation (2) so that *x* is now age (Ma) and *y* is depth (mbsf) (Figure 3):

Equation (1): $y = 0.0237x + 20.126$

Equation (2): $y = 42.194x - 849.2$

The depth (*y* in Equation (2)) or 552.2 mbsf and age 33.2 Ma of Sample 53R-3 was used to calculate the age (*x* in Equation (2)) of each sample. The top of Section 53R-1 at 549 mbsf is dated ~33.1 Ma. The top of section 54R-4 at 563.38 mbsf is dated ~33.5 Ma. This age model is only slightly different from the age models used in Houben et al. (2013) and López-Quirós et al. (2019).

1.3.2 Lithology of Cores

Based on the "Shipboard Scientific Party" report (Barker et al., 1988), unit VII is divided into four subunits based on texture and composition (Figure 4). Cores 53R and 54R are located in Subunit VIIB which is largely comprised of dark olive gray to black claystone, clayey mudstone, and dark gray and dark olive gray silty mudstone (Barker et al., 1988). The sediment composition from 521.7 to 645.6 mbsf, including Cores 53R and 54R, is comprised mostly of terrigenous sediments. Diatoms are completely absent from the sediment or are negligible at less than 10% of the sediment composition. Devitrified volcanic ash and glass components are also present from 510.7 to 597.2 mbsf, including Cores 53R and 54R. Sample 53R-1 contains small amounts of dark gray glauconitic sandy mudstone, but glauconite abundance is less than 2% throughout the rest of the subunit. Rare amounts of silicic benthic foraminifera (*Cyclammina* sp.) are present in Core 54R, which cannot be fully identified due to deformation of the specimens. Bioturbation ranges from minor to dominant, decreasing upcore. Other sedimentological features of Subunit VIIB include fine lamination observed in siltstones, pyrite nodules up to 2 cm in diameter, and sedimentary dropstones less than 2 cm in diameter in Cores 53R and 54R. Clay minerals are predominantly smectite (60% to 100%) with a lesser abundance of illite (5% to 55%), and rare, but still present amounts of chlorite and kaolinite (5% to 30%) (Barker et al., 1988).

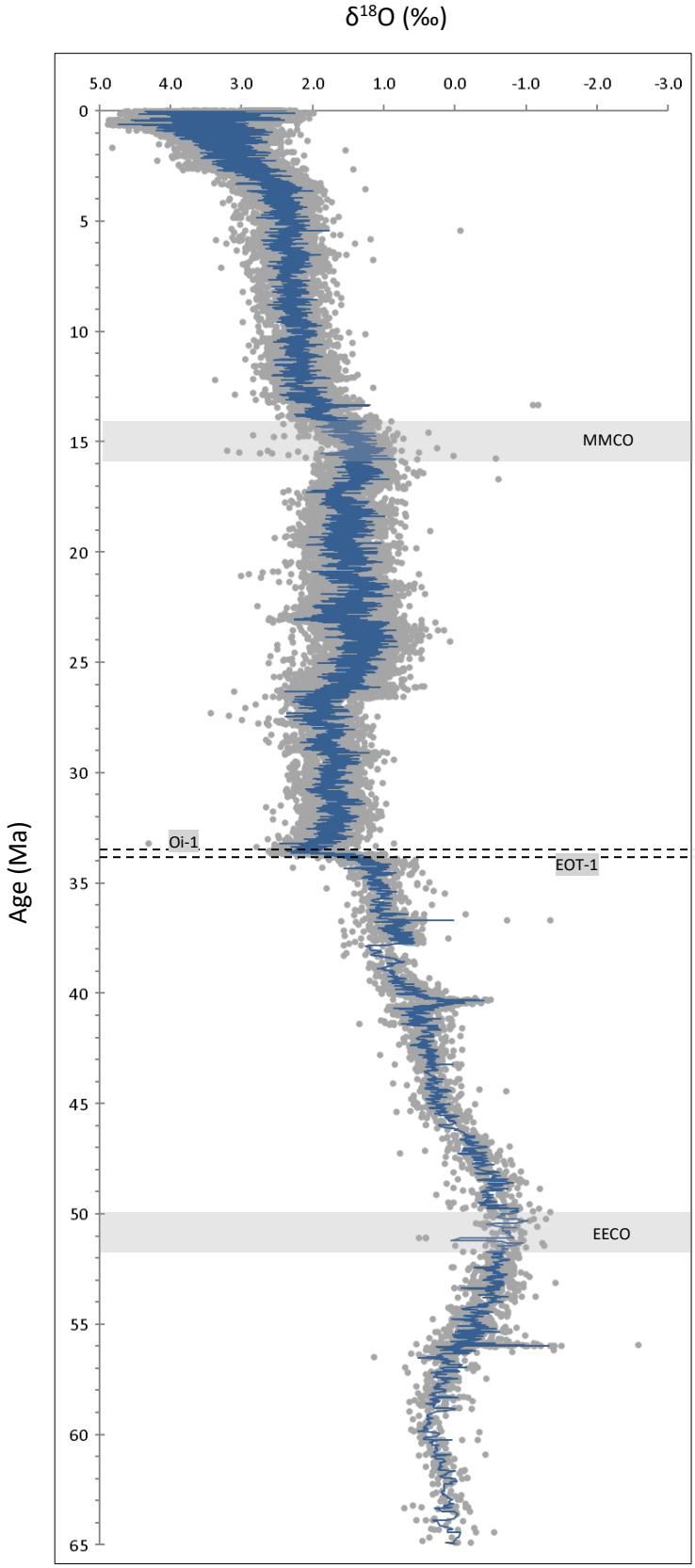

Figure 1: Age (Ma) versus $\delta^{18}O$ (‰) and highlighting global events: EECO from 52 to 50 Ma; EOT-1 at 33.8 Ma with $\delta^{18}O$ increase of 0.9‰ and global cooling of 2.5°C; Oi-1 at 33.545 Ma with $\delta^{18}O$ increase of 1‰ and global cooling of 2°C; MMCO at 15 Ma (Katz et al., 2008); $\delta^{18}O$ data from Veizer and Prokoph (2015).

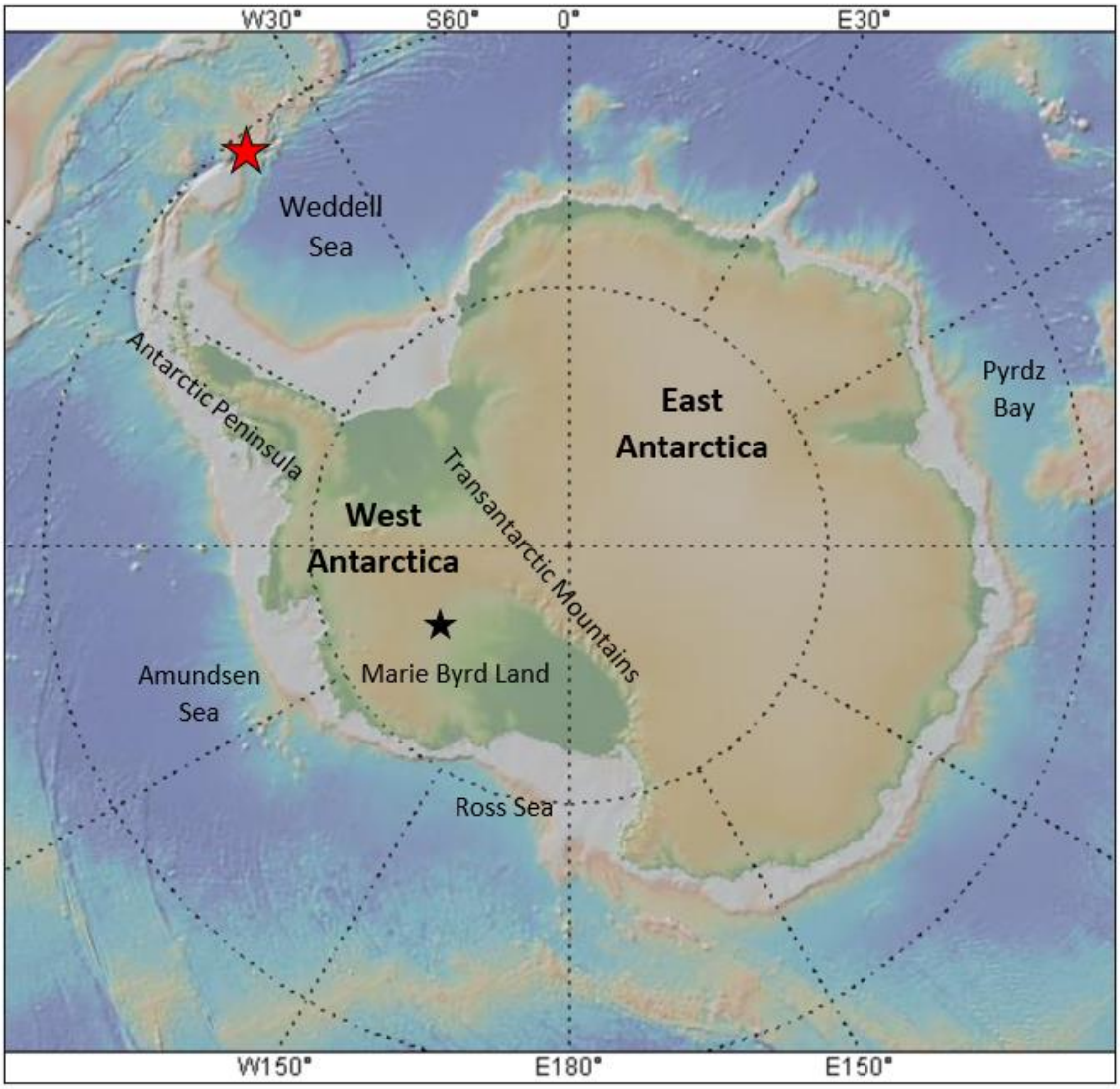

Figure 2: Map of Antarctica with select features. Three broad regions of West Antarctica include: (1) the Ross Embayment, and West Antarctic rift system (WARS), and Marie Byrd Land dome; (2) the Antarctic Peninsula and the Thurston Island Crustal Block; and (3) the Weddell Sea region comprised of the Ellsworth-Whitmore Mountains, Haag Nunataks, and the shallow marine Weddell Sea rift system. The SOM lies in the northwest Weddell Sea sector (Jordan et al., 2020). The red star shows the location of ODP Site 696 on the SOM in the northwestern Weddell Sea. The black star shows the location of Byrd Station. GeoMap App map created using the Global Multi-Resolution Topography (GMRT) synthesis at http://www.geomapapp.org (Ryan et al., 2009).

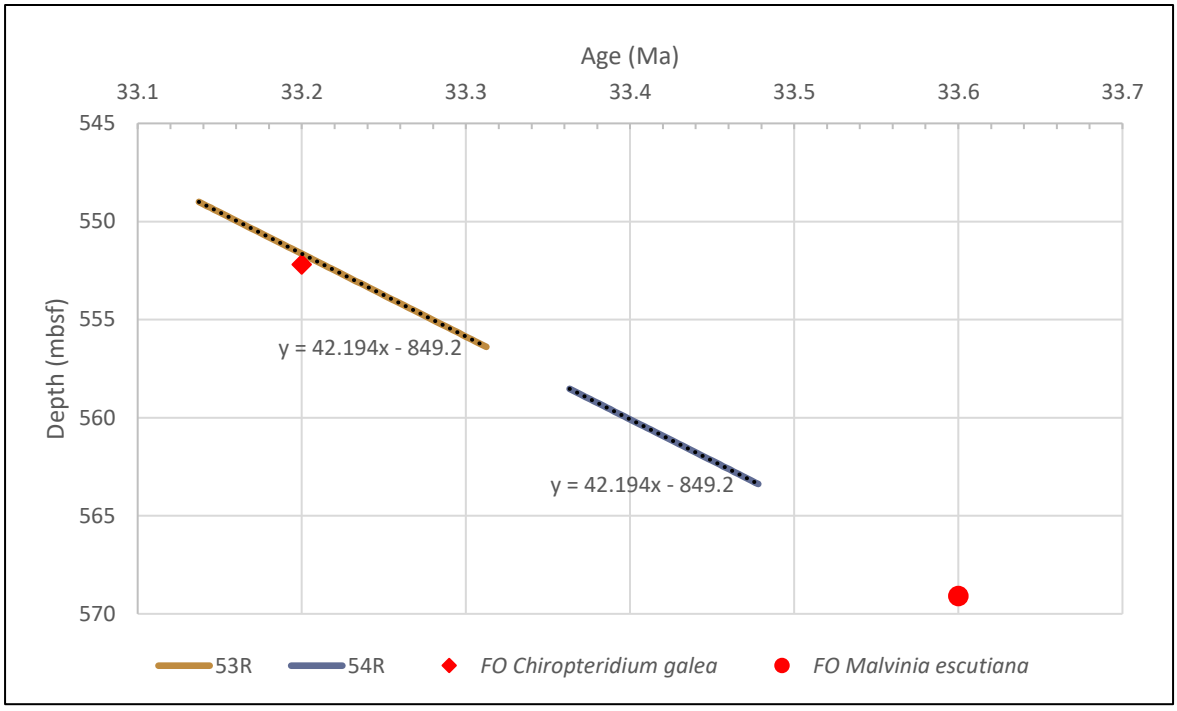

Figure 3: Age model constructed for Cores 53R and 54R using excel based on FO *Chiropteridium galea* at 552.2 mbsf in Section 53R-3 and FO *Malvinia escutiana* at 569.10 mbsf in Section 55R-1 (not studied in this research) (Houben et al., 2013).

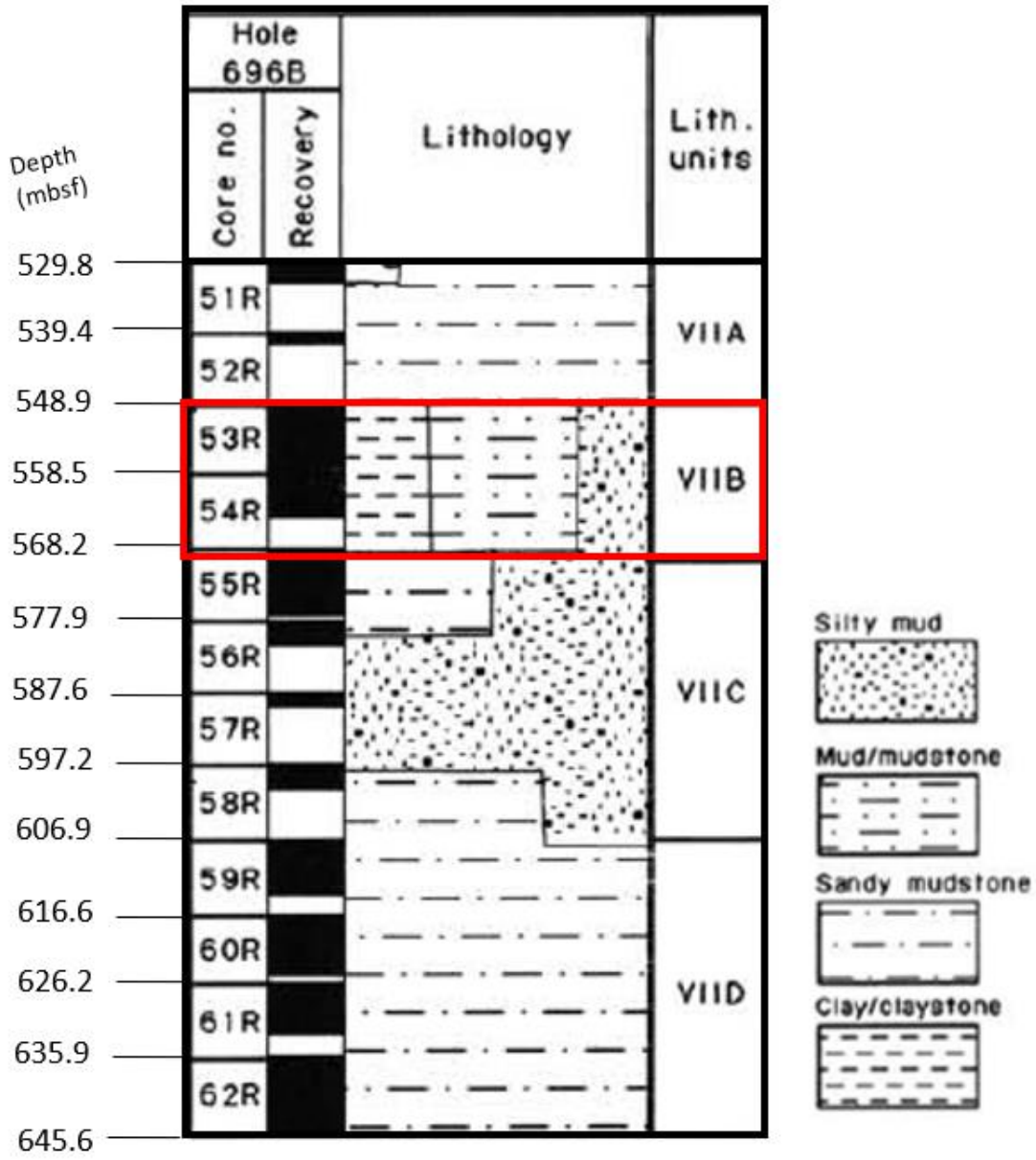

Figure 4: Lithostratigraphic summary with depth (mbsf) for Unit VII of Core 696B, highlighting Cores 53R and 54R studied in this research. The lithology for Cores 53R and 54R is predominately silty mud, mud/mudstone, and clay/claystone. Adapted from the lithostratigraphic summary for Cores 696A and 696B from Barker et al. (1988).

2. METHODOLOGY

Fluctuations in ice-rafted debris (IRD) abundance can reveal changes in the growth and decay of ice sheets (St. John et al., 2014). IRD can be inferred through studies on provenance, grain size, and microfeatures. It is difficult to correctly identify IRD based on any one of these methods alone; all three will give the most accurate classification and historical record. Grain size analysis contributes a multitude of properties of a core section and gives insight into depositional environment, sea level, and weathering rate. However, grain size alone does not provide a comprehensive record, and cannot distinguish between iceberg rafted debris (IBRD) and sea-ice rafted debris (SIRD). Analyzing microtextures of quartz grains can show the physical mechanisms and dynamics of glacial transport. This research focuses on grain size and microtextural analysis for Cores 53R and 54R.

2.1 Sedimentological Analysis

The first method used in this study was the laser particle size analysis to determine the volume percentage of sediment size classes identified in the sediment core samples. This is crucial as the first step to identifying IRD because grain size distribution in a sample is a proxy for the origin of sediments. In addition, this information provides insight to the depositional environment of the grains (St. John et al., 2014).

2.1.1 Sample selection

The sediment core samples used were previously obtained from the International Ocean Discovery Program (IODP) at Texas A&M University and are currently located at Montclair State University. A total of 113 samples were analyzed in the laser particle sizer at Montclair State University. This includes 44 samples from Core 696B-54R and 69

samples from Core 696B-53R. Each sample was sectioned by two-centimeter intervals. Since further analysis on only selected samples was to be completed, the laser particle size analysis was performed for every sample in Cores 53R and 54R to ensure an accurate and comprehensive characterization prior to selection of a subset of samples for additional examination (Figure 5).

2.1.2 Sample preparation

To prepare samples for laser particle size analysis, the methodology from Martin Konert and Jef Vandenberghe was followed (Konert and Vandenberghe, 1997). A fragment of approximately 1 cm in length was obtained for each sample. When possible, the fragment was taken directly from the original sample. A mortar and pestle was used by applying vertical pressure to prevent damage of grains if compaction of the sediment made it difficult to separate a fragment by hand. Each sample was placed in a 250 mL beaker with 10 mL of 30% H_2O_2 and the beaker was filled to a volume of 50 mL with Millipore water. A swirling motion was applied to the beaker to allow disaggregation of the particles. Most samples were placed in the ultrasonic bath for at least 10 minutes, or as needed, to further disaggregate the sediment. Subsequently, the beakers were moved to hot plates. Once boiling occurred, 2 mL of 10% HCl was added to each beaker to remove any organic matter that may be present to leave only mineral detritus. Once the reaction finished, the solution was boiled until the volume was less than 50 mL and then was removed from heat to cool.

The suspension was transferred to a 50 mL vial, placed in the centrifuge, and spun for 30 minutes at 2000 rotations per minute (rpm). After the suspension separated into solid and liquid, the liquid was carefully discarded leaving only the residuals. Next, the vial was

filled to 50 mL with Millipore water, shaken to wash the solid, and once again spun for 30 minutes at 2000 rpm in the centrifuge. Then, each sample was placed in its original beaker with 50 mL of Millipore water and ½ teaspoon of sodium pyrophosphate to disperse the sediments. The beakers were returned to the hot plates to dissolve the sodium pyrophosphate.

2.1.3 Data Acquisition

Once samples were prepared, the Malvern Mastersizer 2000 (which is located at Montclair State University in the Department of Earth and Environmental Studies) was used to determine the particle size distribution of a sample using a laser system. It contains a red laser, a blue light source, side scatter detectors, back scatter detectors, and focal plane detectors. A laser beam hits the samples, and the detectors measure the light intensity that is calculated based on angles of the scattered light. This information was processed in a computer program that analyzes the grain size distribution. Two light sources with different wavelengths are used in the laser system, a blue and red light.

The particle size analyzer first measures the background of about 750 mL of Millipore water in a 1000 mL beaker. Then, the sample was added to the beaker, three measurements are taken, and the average of the three measurements was calculated (Malvern Instruments Ltd., 2007). In some cases, anomalous results were due to high obscuration of the laser, meaning large amounts of sediment in the sample. Therefore, some samples were diluted with Millipore water as the sample was continuously rotated by the Hydro 2000MU pump accessory. This is to ensure consistent dispersion in the sample, as well as random sampling of the suspended material by the laser (Sperazza et al., 2004). A full list of samples diluted is included in the appendix (Table A.1). After each sample was

measured, the sample was discarded, and the instrument was flushed with Millipore water to avoid contamination between samples.

Results from laser particle size analysis was integrated into Microsoft Excel spreadsheets which included the technical data of each measurement taken such as the obscuration and concentration of the sample. The Mastersizer 2000 detects particle sizes in a range of 0.02 to 2000 micrometers (µm) (Sperazza et al., 2004). The Wentworth Grain Size Classification was used for this project and it classifies clay particles as less than 4 µm, silt particles between 62.5 and greater than 4 µm, sand particles between 2,000 and greater than 62.5 µm, and gravel particles greater than 2,000 µm (Wentworth, 1922).

2.1.4 Sedimentological Properties

Particle size data was used to calculate the IRD mass accumulation rate (MAR) which can be used to infer the abundance of calving icebergs over a drillsite through time. The equation used for IRD MAR, in $g/cm^2/kyr$ (St. John, 2008):

$$\text{IRD MAR} = \text{CS\%} \times \text{DBD} \times \text{LSR} \times \text{TERR}$$

where CS% is the volume percentage of grains >150 µm, using > 125 µm obtained from particle size data; DBD is the dry bulk density (g/cm^3) and was obtained from the "Shipboard Scientific Party" report (Barker et al., 1988) using method B; LSR is the linear sedimentation rate (cm/kyr) is obtained from the age model and TERR is the terrigenous fraction. The carbonate fraction is considered negligible since little reaction to the hydrochloric acid occurred during preparation of the samples for particle size analysis and with a lack of other biogenic components TERR is estimated to be around 1 for all samples.

Uniformity is measured using the ratio of D60/D10, where D60 is the diameter greater than 60% of sediments and D10 is the diameter greater than 10% of sediments. This value was recorded in the output data file for the laser particle size analysis. Uniformity indicates poorly sorted sediments which designates increased glacial activity. (Passchier et al., 2018). Sortable silt and mean sortable silt were assessed to determine the effect of current sorting on the sediments where r > 0.5 indicates current sorting is involved in the sedimentation process for mean sortable silt. Using the Reduced Major Axis in the Paleontological Statistics (PAST) Software Package (Hammer et al., 2001) and particle size data, the equations for sortable silt and mean sortable silt are:

$$SS\ \% = \frac{\%\ 10 \text{ to } 63\ \mu m}{\%(< 63\ \mu m)} * 100$$

$$\overline{SS} = \frac{1}{V}\sum_{i=1}^{256}(V_i * d_i)_1$$

where d_i is the midpoint value of the *i*th size bin (*i*= 1, 2, 3, …, 256) between 10 µm and 63 µm, v_i is the total volume of all the grains that fall into the *i*th size bin, and v is the total volume of all grains measured per sample (Tegzes et al., 2015). Using the Weddell/Scotia calibration equation from McCave et al. (2017), scalar flow speed was calculated from mean sortable silt to estimate the flow speed of bottom currents.

$$U = \frac{\overline{SS} - 12.23}{0.59}$$

where U is scalar flow (cm/s) and $\overline{SS}$ is mean sortable silt (McCave et al., 2017). Some sections received a low obscuration during Laser Particle Size analysis, where air bubbles may have formed that display a false large volume percentage of coarse grains. These

results were removed from further grain size analysis and are not displayed in figures (full list of samples listed in Table A.2). A sample with an obscuration deemed too low for further analysis is a value < 6% (Malvern Instruments Ltd., 2007).

2.2 Physical Analysis

2.2.1 Sample Selection

Based on results from the laser particle analyzer, five samples were chosen for imaging using a Scanning Electron Microscope (SEM) to assess the presence of ice-rafted debris based on surface texture analysis. The samples selected exhibited large volume percentages of grain sizes greater than or equal to 150 µm, relative to the rest of the samples in the section, since IRD is most often greater than or equal to 150 µm. Furthermore, core descriptions from the expedition log were used to eliminate samples which included pyrite nodules, which gives a misrepresentation of IRD grains in a sample. Ten samples were selected for sieving, which was then narrowed down to five samples for SEM analysis.

2.2.2 Sample Preparation

The first step to prepare for SEM analysis is to sieve the samples, 10 of which were chosen based on the factors stated in the paragraph above. A sample tin was weighed, and new samples were gathered from the sample bags and placed in the weighing tin. The weight of the sample was subtracted from the weight of the tin plus the weight of the sample and recorded. Next, the sample was placed in an evaporation dish with Millipore water to disaggregate the sample. When necessary because of compaction, the samples were transferred to 150 mL beakers and placed in the ultrasonic bath for at least one hour. Some samples required further time to disaggregate and were left in Millipore for up to one week

before sieving. After complete disaggregation, the sample was placed in a sieve for grains greater than 150 µm. Using a funnel, Millipore water, and a rubber policeman, the sample was washed thoroughly through the sieve, leaving only grains greater than 150 µm. The sample was dried in the oven at 60°C overnight to evaporate the moisture. Then, a weighing tin was weighed, and the weight was recorded. The sample was placed in the tin and weighed, and the weight of the tin was subtracted from the weight of the tin plus the weight of the sample. This yields the weight of grains greater than 150 µm. The sand fraction was obtained by dividing the weight of the grains greater than 150 µm by the weight of the original sample.

Five of 10 sieved samples were selected for SEM analysis, based on the greatest yield of grains greater than 150 µm (Table 1). Using a microscope and tweezers, about 40 grains per sample that resembled quartz grains under the microscope were placed on the specimen setting for SEM. The specimen setting consisted of a 15 mm high and 5 mm diameter aluminum mount with double sided carbon tape placed on top. The grains were placed on the carbon tape, and the specimen setting was coated with gold. Gold coating was used for its ability to obtain high resolution imaging due to its high conductivity and less interference with the scattered electrons (Damiani et al., 2006).

2.2.3 Data Acquisition

The SEM used was the Hitachi S-3400N SEM with Bruker BSE detector, which is operated in the Microscopy and Microanalysis Research Laboratory at Montclair State University. Secondary Electron Imaging at 15 kilovolts voltage was used for SEM analysis. Furthermore, Energy Dispersive Spectroscopy (EDS) was applied to each grain to determine the elemental composition and to identify quartz for IRD microtexture

assessment. XY graph results from EDS were displayed as images and integrated into Microsoft Excel spreadsheets. Microtexture analysis is based on microfeatures identified in Dunhill (1998) and St. John et al. (2014), and grain roundness was compared visually to SEM images from Powers (1953).

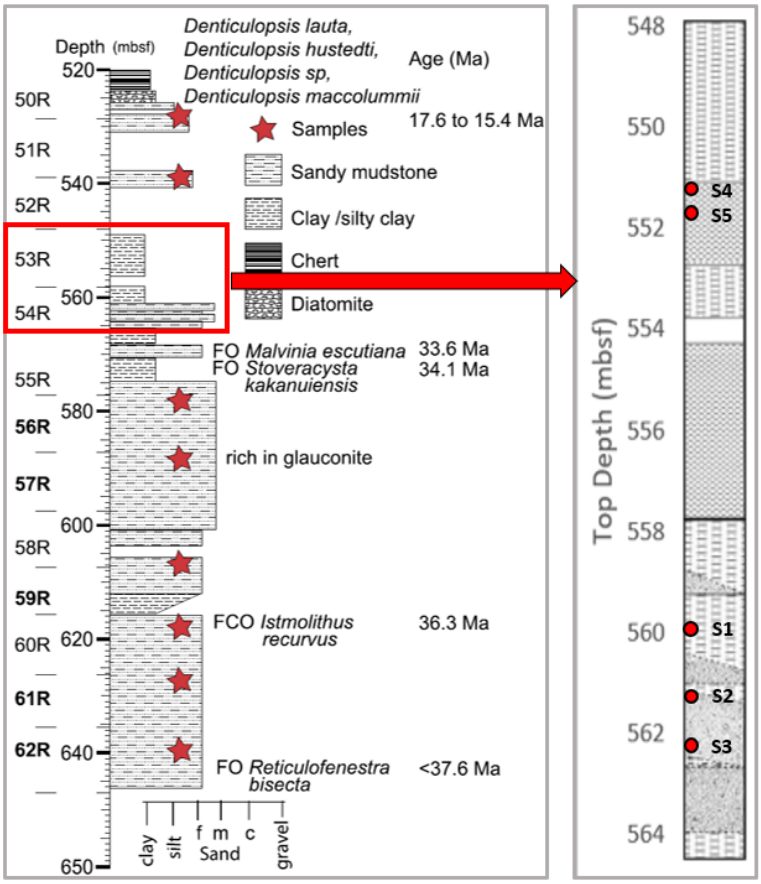

Figure 5: Stratigraphy and age controls for Hole 696B, modified to enlarge 53R and 54R (adapted from Carter et al. (2016) with stars denoting sample depths studied by Carter et al. (2016)). Detailed lithologic log on the right adapted from Barker et al. (1988). Red circles on lithologic log are labeled S1-S5 and were analyzed with SEM where S4 and S5 are from Core 53R and S1-S3 are from Core 54R.

Sample #	Sample Name
S1	113-696B-54R-2-63-66
S2	113-696B-54R-3-22-25
S3	113-696B-54R-3-126-129
S4	113-696B-53R-2-88-91
S5	113-696B-53R-3-1-4

Table 1: Samples from Cores 53R and 54R that were analyzed with SEM and are referred to as S1-S5 in this research.

3. RESULTS

3.1 Grain Size

3.1.1 Grain Size Distribution

Laser Particle Size analysis shows that silt is the dominant grain size (>50%) in most samples of Core 53R except for 9 samples where the volume percentage of silt is between 41% and 49%. In Core 54R, silt is the dominant grain size (>50%) in almost all samples except for 1 sample where the volume percentage of silt is ~43%. When plotted on a ternary diagram, it is easy to see that silt is the dominant grain size in Core 54R but also the grain size distribution appears uniform (Figure 6). However, in Core 53R, there is more variance. When plotted against depth, there is a fining upward trend for Core 54R and a coarsening upward trend for Core 53R (Figure 11a). The volume percentage for silt increases upcore in Cores 53R and 54R. Grain size distributions for each section of Core 53R and 54R with the average volume percentage of sand, silt, and clay are shown in Figures 7 and 8.

Grain size distribution graphs of volume percentage for each core section were created to display abrupt increases (“tails”) or a larger distribution of coarse grains in order to determine which samples should be further considered for SEM analysis. Sample 53R-5-34-37 is an example for further consideration for SEM analysis (Figure 9). Some sections displayed these features but were not considered for SEM analysis. This is because some sections containing pyrite nodules display a large volume percentage of coarse grains that are not detrital sand, such as Sample 53R-5-99-102 (Figure 9). Additionally, high

percentages of sand within layers of a finer fraction can indicate IRD transported by glaciers and then entrained in currents.

3.1.2 Sand Fraction

Sand fraction for sieved samples is between <1 wt. % and 6 wt. % for Core 53R and between <1 wt. % and 18.4 wt. % for Core 54R. There is a decreasing trend upcore for Core 54R. At 562.74 mbsf, (Sample 54R-3-126-129) the sand fraction is 18.4 wt. %. This differs from the ship's lithology column which shows an abrupt change from clayey mud and mud/mudstone to silty mud, and then back to clayey mud and mud/mudstone (Barker et al., 1988) (Figure 10).

3.1.3 Additional Attributes

The Uniformity Coefficient measures the degree of sorting for sediments where numbers >4 specify poorly sorted sediments (Houben et al., 2013). In Core 54R, the average uniformity for each section fluctuates between ~1.9 and ~3.5, except for Section 54R-3 where the average uniformity is ~4.8. Core 54R has 12 samples which are poorly sorted with a maximum value of 15.4 in Section 54R-3. However, Core 54R has an overall average uniformity value of 3.5 and is considered well sorted. In Core 53R, the average uniformity for each section fluctuates between ~1.5 and ~2.4, except for Section 53R-5 where the average uniformity is ~4.3. Core 53R has 5 samples which are poorly sorted with a maximum uniformity value of 23.9 in Section 53R-5. However, Core 53R has an overall average uniformity value of 2.3 and is considered well sorted. Also, many of the spikes in uniformity coincide with spikes in volume percentage of coarse fraction >150 μm. It is

difficult to discern a trend upcore, but overall, Core 54R can be considered less sorted than Core 53R (Figure 11d).

From the age model, a Linear Sedimentation Rate (LSR) of 4.22 cm/kyr for Cores 53R and 54R was obtained. IRD MAR displays multiple peaks throughout Core 54R with a slight decreasing trend upcore. The values range from a minimum of 0 $g/cm^2/kyr$ at Sample 54R-1-3-6 to a maximum of 1.8 $g/cm^2/kyr$ at Sample 54R-3-32-35. The average IRD MAR for Core 54R is 0.35 $g/cm^2/kyr$. Core 53R displays an abundance of peaks throughout with no visible trend. The values range from a minimum of 0 $g/cm^2/kyr$ at 7 different samples to a maximum of 2.1 $g/cm^2/kyr$ at Sample 53R-5-53-55. The average IRD MAR for Core 53R is 0.17 $g/cm^2/kyr$. The peaks mostly coincide with large volume percentages of sand. For example, Sample 54R-3-22-25 displays a peak IRD MAR of 1.8 $g/cm^2/kyr$, sand volume of ~30%, and IRD was identified using SEM.

Sortable silt was assessed to determine the effect of current sorting on the sediments (Figure 12b) where $r > 0.5$ indicates current sorting is involved in the sedimentation process. The r values are 0.73 for Core 53R and 0.69 for Core 54R (Figures A.1(a) and A.1(b), respectively). Therefore, since the r values are greater than 0.5, current sorting is involved in the sedimentation process. The scalar flow speed of bottom currents was estimated using mean sortable silt to identify climate trends. The average flow speeds for Cores 54R and 53R are ~23.4 cm/s and ~21.6 cm/s, respectively. While Core 54R has a faster average flow speed, Core 53R has a faster maximum flow speed at 38 cm/s compared to 30.4 cm/s for Core 54R (Figure 12a).

3.2 Surface Textures

Table 2 displays the categories and specific microfeatures analyzed in this research with the corresponding number of grains for samples 1-5. Roundness is divided into angular, sub-angular, sub-rounded, and rounded (Powers, 1953); shape is divided into equant, elongate, irregular, and tabular (flat); relief is divided into low, medium, and high. Surface textures are based on fractures, silica dissolution, or miscellaneous microfeatures where fractures include breakage blocks, conchoidal fractures, step-like fractures (Figure 13), and isolate cusps (St. John et al., 2014). Silica dissolution is considered as little to none (0 to <25%), some (>25% to <75%), and most (>75% to ~100%). Miscellaneous microfeatures include striations and microlayering.

For this study, seven different types of grains were observed based on grain microfeatures (Figure 14). Grain Type 1 characteristics include rounded/sub-rounded, low relief, little to no silica dissolution, and little to no fractures. It is determined not to be glacially influenced and, therefore, not an IRD type of grain. Grain Type 2 characteristics include rounded/sub-rounded, low/medium relief, some or most silica dissolution, and little to no fractures. Grain Type 3 characteristics include sub-rounded/sub-angular, low/medium relief, some or most silica dissolution, and fractures present. Grain Type 4 characteristics include rounded/sub-rounded, low/medium relief, little to no silica dissolution, and fractures present. Grain Type 5 characteristics include angular/sub-angular, low/medium relief, little to no silica dissolution, and fractures present. Grain Type 6 characteristics include angular/sub-angular, medium/high relief, some or most silica dissolution, and fractures present. Grain Type 7 characteristics include angular/sub-angular, medium/high relief, some or most silica dissolution, little to no fractures.

As shown in Table 2 displaying the grain types identified, 35% of grains are placed into Grain Types 4 and 5, representing iceberg rafted debris (IBRD). 60% of grains are placed into Grain Types 2, 3, 6, and 7, which could be representing sea-ice rafted debris (SIRD) because of the lack of fresh fractures and abundance of silica dissolution (cf. St. John et al., 2014). 5% of grains are neither SIRD nor IBRD since they are not considered to be glacially influenced but could have originated from abrasion in a non-glacial environment. Figure 15a displays the overall percentage of SIRD versus IBRD grain types in Cores 53R and 54R. Figure 15b displays the percentage of each grain types 1-7 for Cores 53R and 54R. Figure 15c displays the grain types per Samples 1 through 5. The ratio of SIRD to IBRD is uniform in sample 3. SIRD grain types are dominant in the rest of samples 1, 2, 4, and 5. Additional figures for microfeatures are included in the appendix (Figures A.2 – A.6).

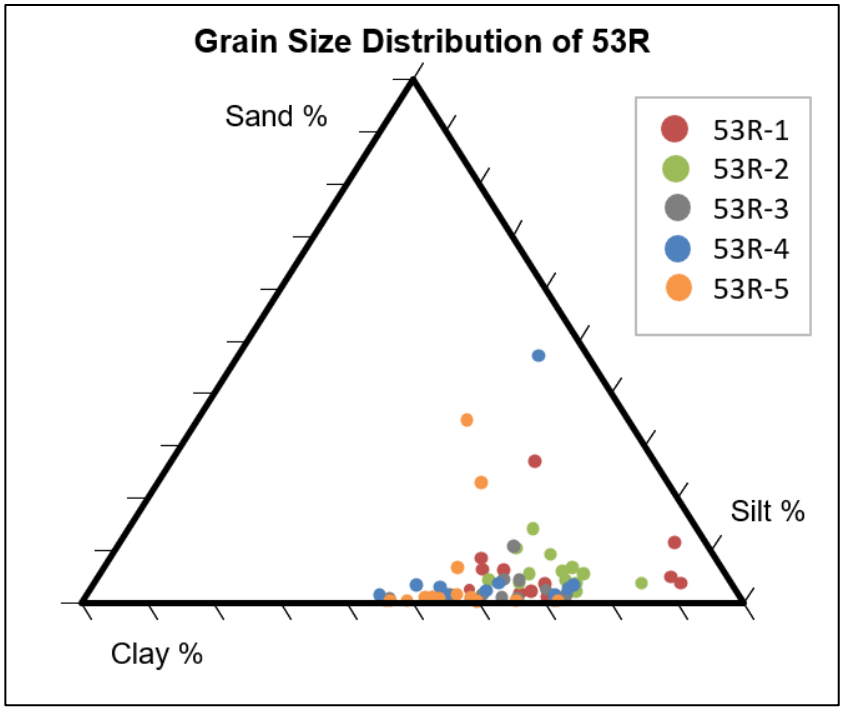

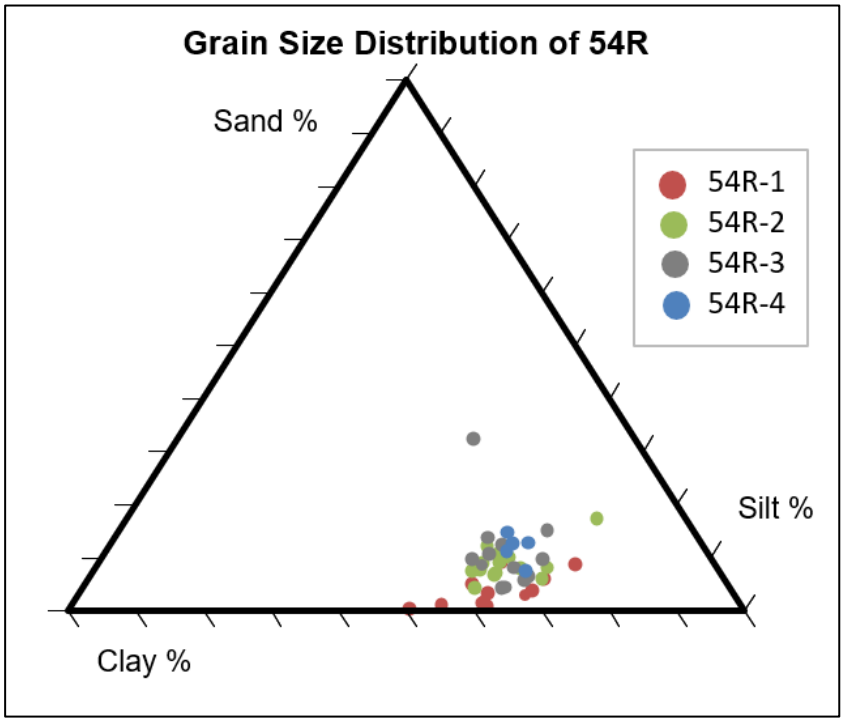

Figure 6: Ternary diagrams of grain size distributions plotted by clay, silt, and sand percentages for Core 53R (sections 1-5) and Core 54R (sections 1-4). In Core 53R, silt is the dominant grain size (>50%) in most samples except for 9 where the volume percentage of silt is between 41% and 49%. In Core 54R, silt is the dominant grain size in almost all samples except for 1 sample where the volume percentage is ~43%. The grain size distribution appears uniform in Core 54R, but there is more variance in Core 53R.

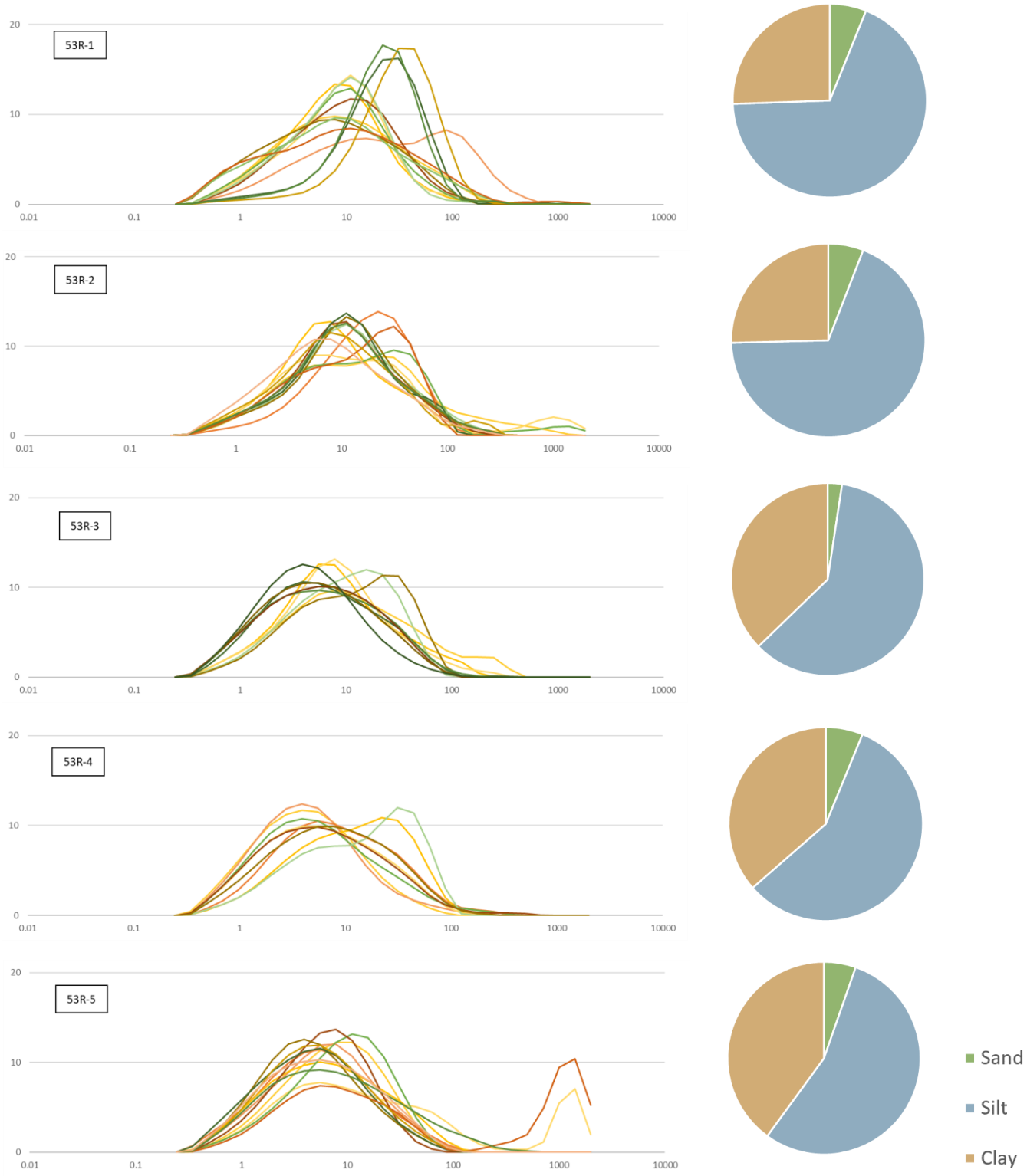

Figure 7: Grain size distribution of 53R sections 1-5, with volume percentage on the y axis and particle size (µm) on the x axis. The average volume percentage of clay, silt, and sand for each section is shown in the pie charts on the right. Silt is the dominant grain size in all sections of Core 53R.

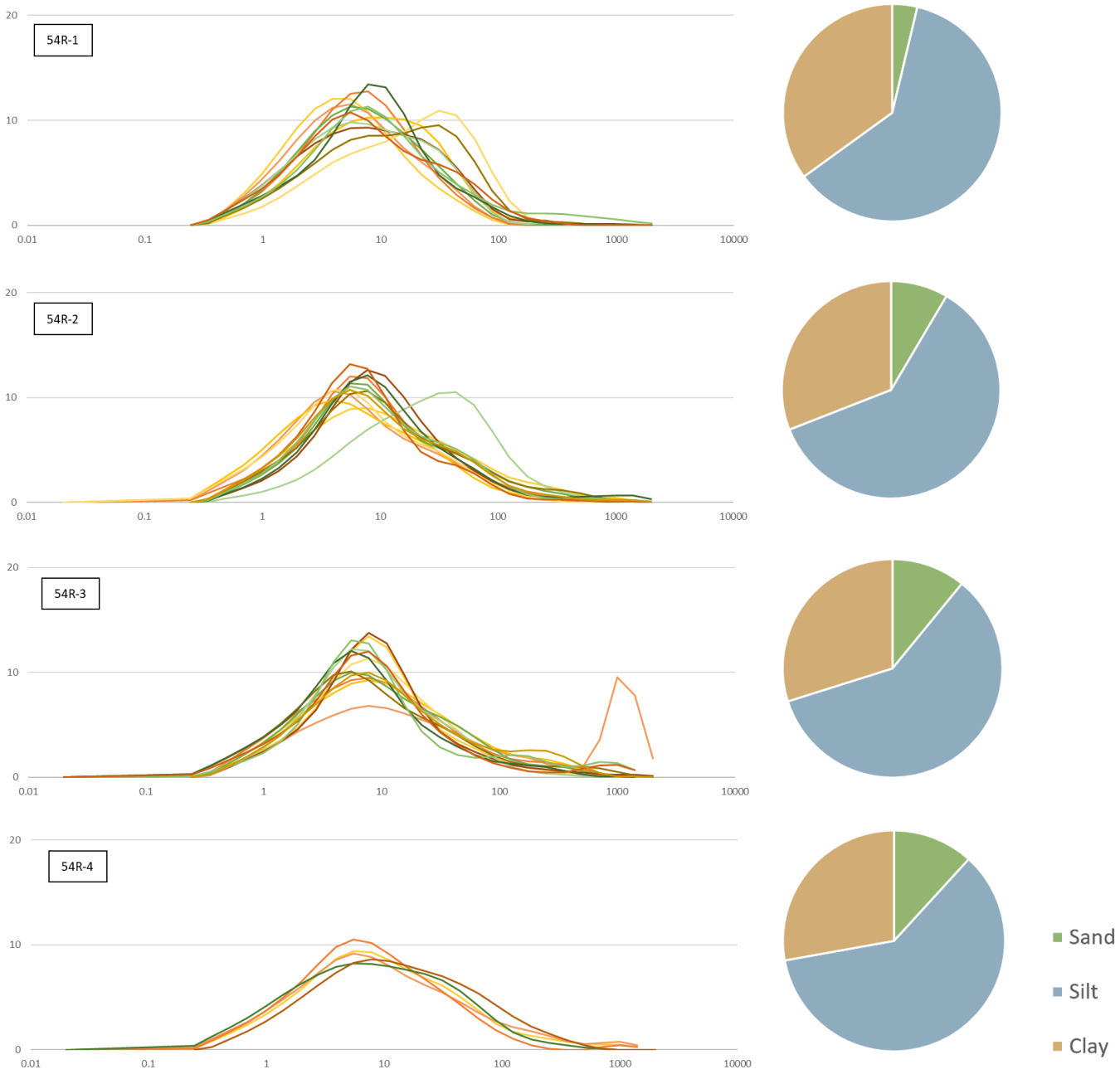

Figure 8: Grain size distribution of 54R sections 1-4, with volume percentage on the y axis and particle size (µm) on the x axis. The average volume percentage of clay, silt, and sand for each section is shown in the pie charts on the right. Silt is the dominant grain size in all sections of Core 53R.

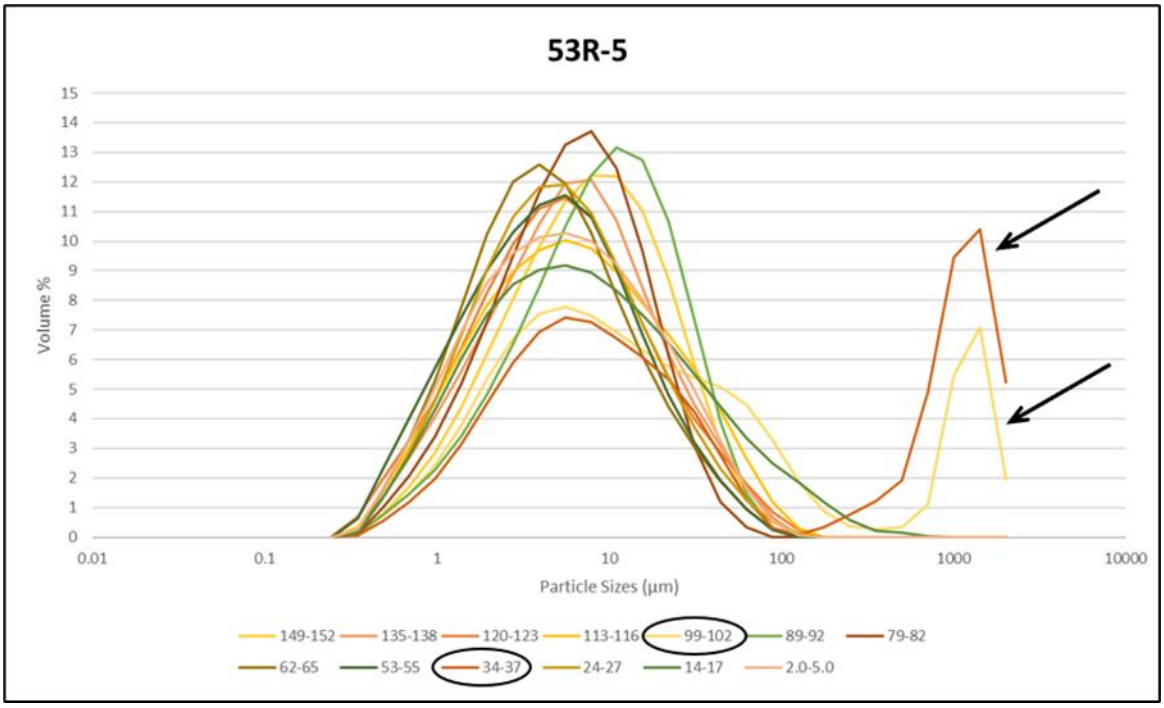

Figure 9: Grain size distribution of section 53R-5. Grain size distribution graphs of volume percentage for each core section were created to display abrupt increases ("tails") or a larger distribution of coarse grains in order to determine which samples should be further considered for SEM analysis. Sample 34-37 was selected for further analysis using SEM. Sample 99-102 displayed a large volume percentage of coarse grains due to the presence of pyrite nodules and therefore, was not selected for further analysis using SEM.

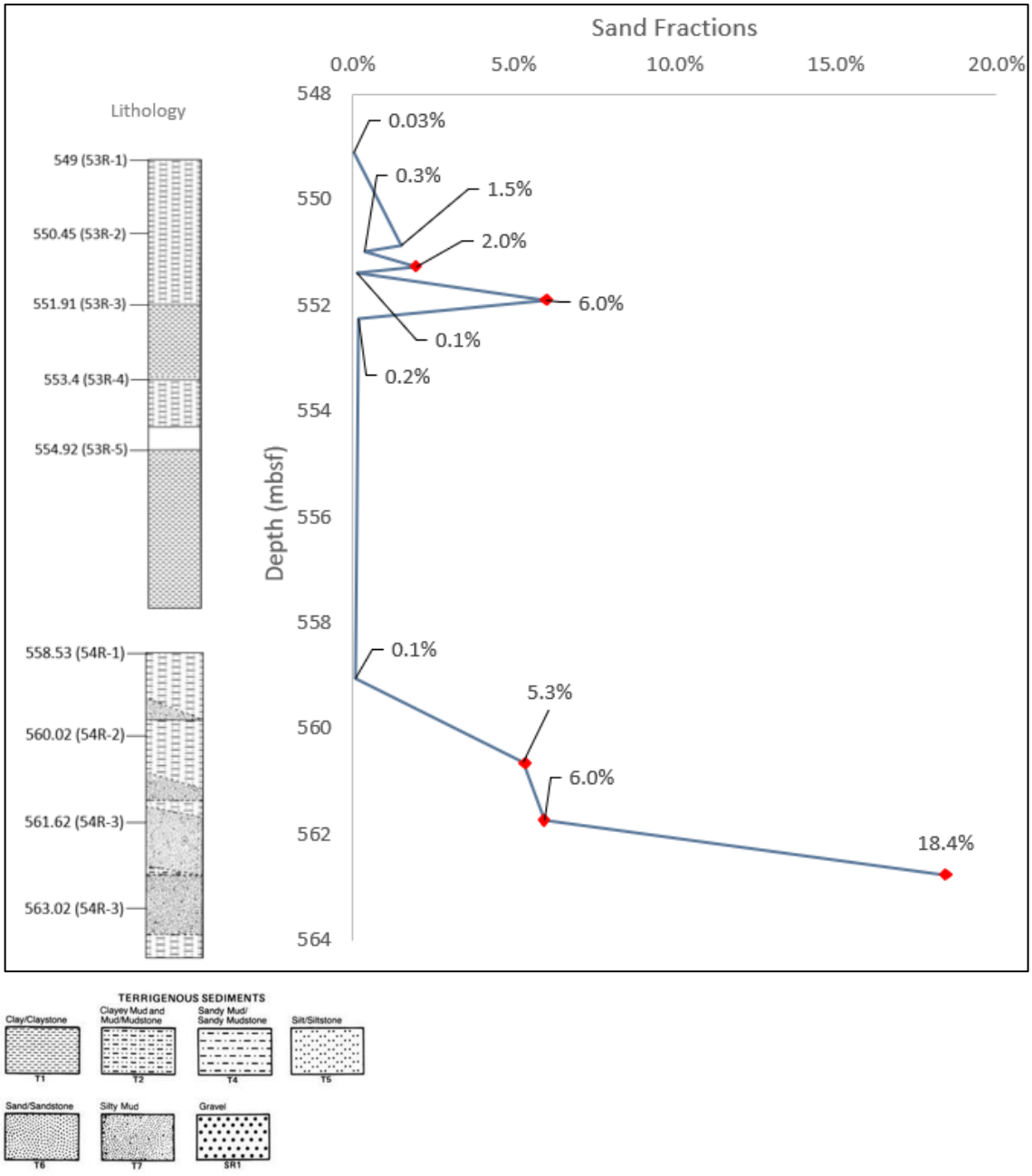

Figure 10: Sand fraction (wt %) plotted against depth (mbsf) for Cores 53R and 54R. Red diamonds represent samples analyzed using SEM – in order from top to bottom of the core – S4, S5, S1, S2, S3. The lithology column is from Barker et al. (1988). There is a decreasing trend upcore for Core 54R. At 562.74 mbsf, (Sample 54R-3-126-129) the sand fraction is 18.4 wt. %. This differs from the ship's lithology column which shows an abrupt change from clayey mud and mud/mudstone to silty mud, and then back to clayey mud and mud/mudstone (Barker et al., 1988).

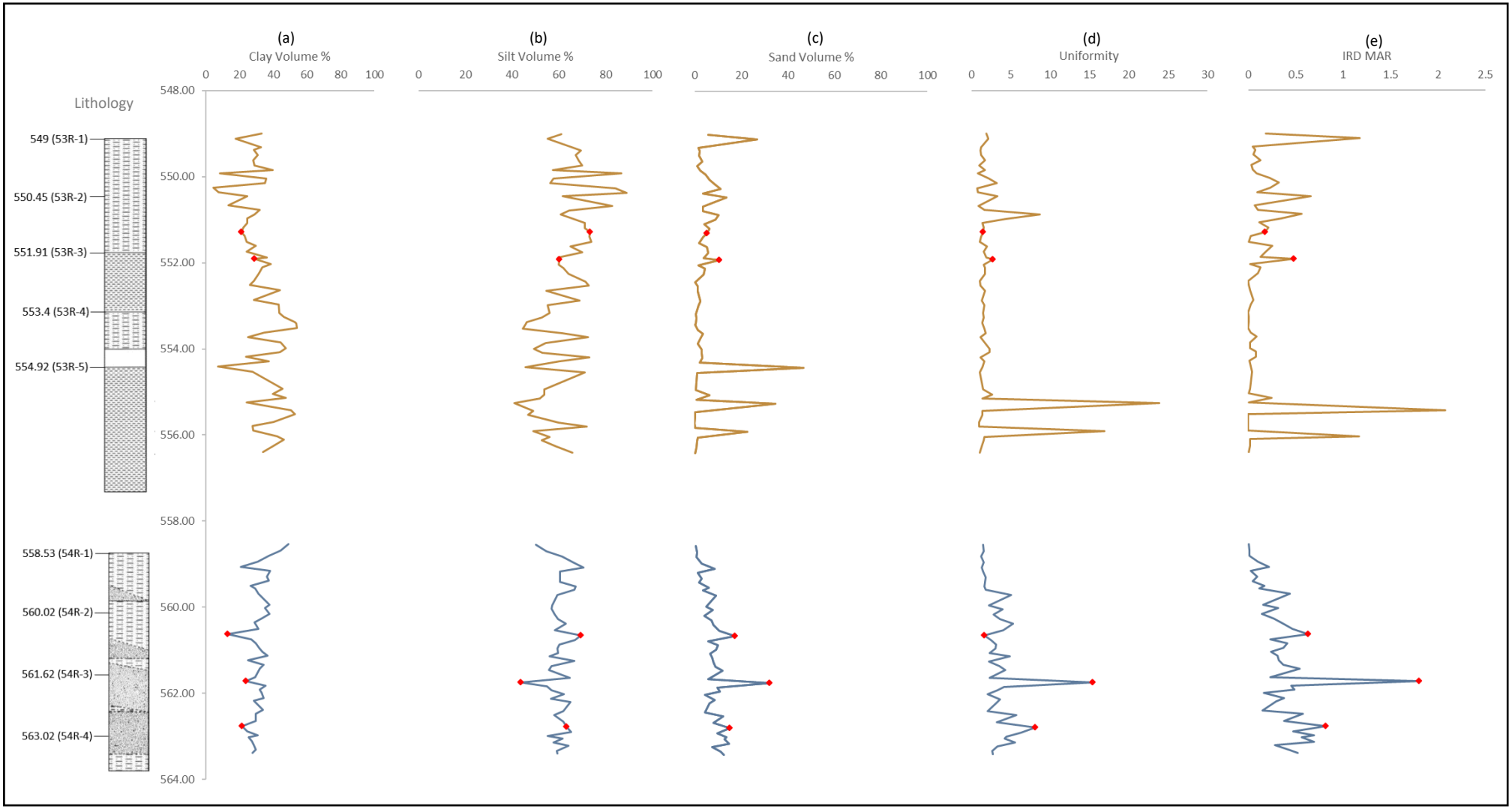

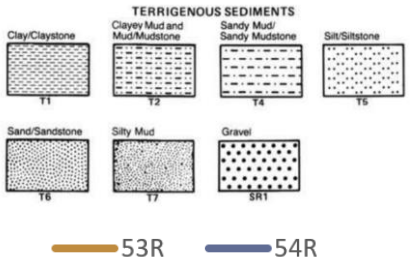

Figure 11: Graphs plotted against depth (mbsf) and lithological core – (a) volume percentage of clay where there is a fining upward trend for Core 54R and a coarsening upward trend for Core 53R; (b) volume percentage of silt; (c) volume percentage of sand; (d) Uniformity where Cores 53R and 54R are considered well sorted; (e) IRD MAR (g/cm2/kyr) where Core 54R displays a decreasing trend upcore, but there is no visible trend for Core 53R. Red diamonds represent samples analyzed using SEM – in order from top to bottom of the core – S4, S5, S1, S2, S3. The lithology column is from the site report – 'Shipboard Scientific Party' (Barker et al., 1988).

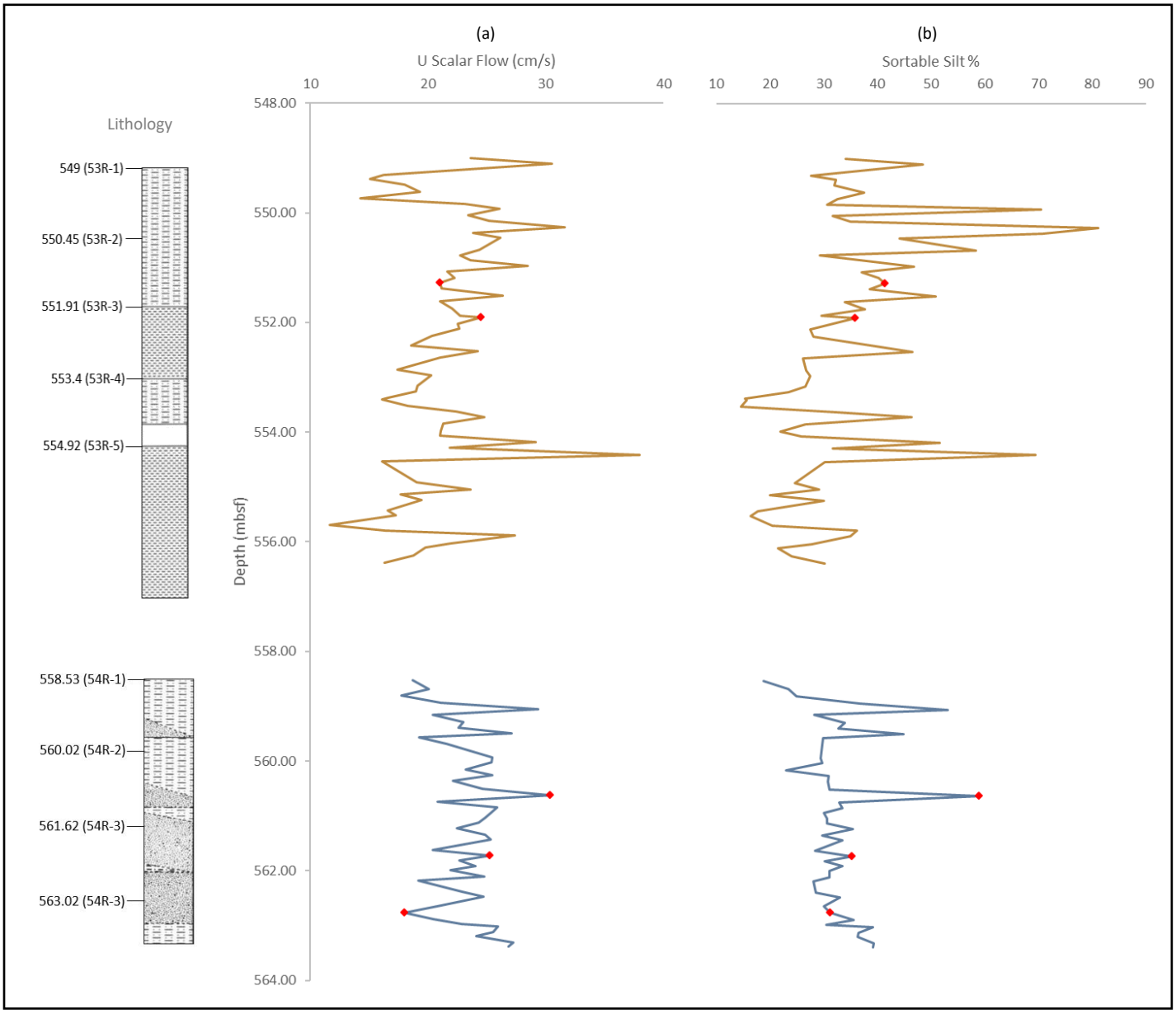

Figure 12: Graphs plotted against depth (mbsf) – (a) U – Scalar Flow (cm/s) obtained from mean Sortable Silt. Core 54R displays a constant scalar flow while Core 53R increases scalar flow upcore; (b) Sortable Silt %. Red diamonds represent samples analyzed using SEM – in order from top to bottom of the core – S4, S5, S1, S2, S3. The lithology column is from the site report – 'Shipboard Scientific Party' (Barker et al., 1988).

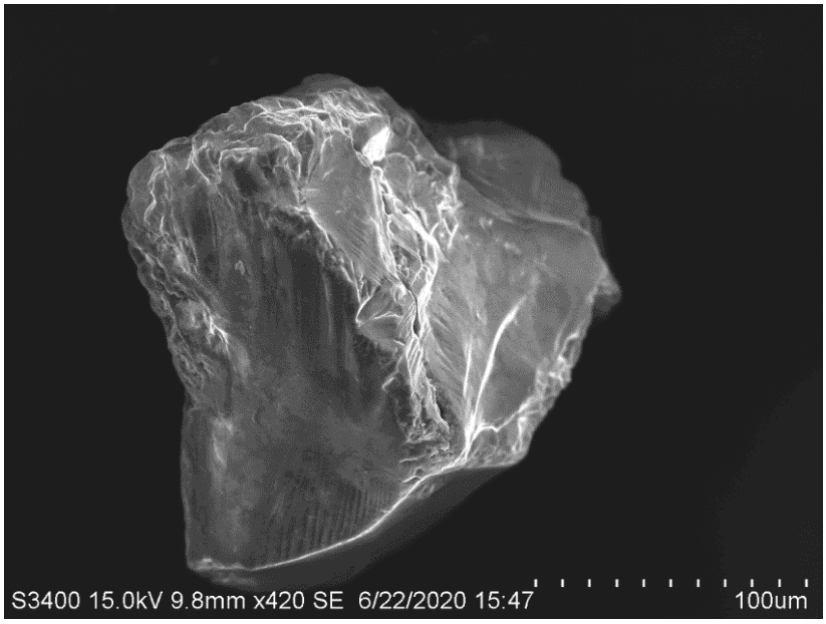

Figure 13: Sample 2-37 of Core 54R was interpretated to be a Type 5 grain and iceberg rafted debris (IBRD). (Type 5, IBRD) with fractured step plates and edge abrasion.

Category	Characteristic or Microfeature	Number of Grains
Roundness	Angular	34
	Sub-angular	36
	Sub-rounded	27
	Rounded	8
Shape	Equant	24
	Elongate	11
	Irregular	64
	Tabular (flat)	6
Relief	High	7
	Medium	61
	Low	37
Surface Texture		
Fractures	Breakage blocks	29
	Conchoidal fracture	20
	Step-like fractures	35
	Isolated cusps	25
Silica Dissolution	Little to none (0 to <25%)	47
	Some (>25% to <75%)	37
	Most (>75% to ~100%)	21
Miscellaneous	Striations	16
	Microlayering	13
Grain Type		
Sea-ice IRD (SIRD) (60%)	2	17
	3	14
	6	19
	7	13
Iceberg IRD (IBRD) (35%)	4	3
	5	34
Not IRD (5%)	1	5

Table 2: Grain microfeatures analyzed in this research which resulted in grouping of seven different types of grains, and further grouped into IRD type – SIRD or IBRD, except for Grain Type 1 which is not considered IRD. Grain Type 1 characteristics include rounded/sub-rounded, low relief, little to no silica dissolution, and little to no fractures. It is determined not to be glacially influenced and, therefore, not an IRD type of grain. Grain Type 2 characteristics include rounded/sub-rounded, low/medium relief, some or most silica dissolution, and little to no fractures. Grain Type 3 characteristics include sub-rounded/sub-angular, low/medium relief, some or most silica dissolution, and fractures present. Grain Type 4 characteristics include rounded/sub-rounded, low/medium relief, little to no silica dissolution, and fractures present. Grain Type 5 characteristics include angular/sub-angular, low/medium relief, little to no silica dissolution, and fractures present. Grain Type 6 characteristics include angular/sub-angular, medium/high relief, some or most silica dissolution, and fractures present. Grain Type 7 characteristics include angular/sub-angular, medium/high relief, some or most silica dissolution, little to no fractures.

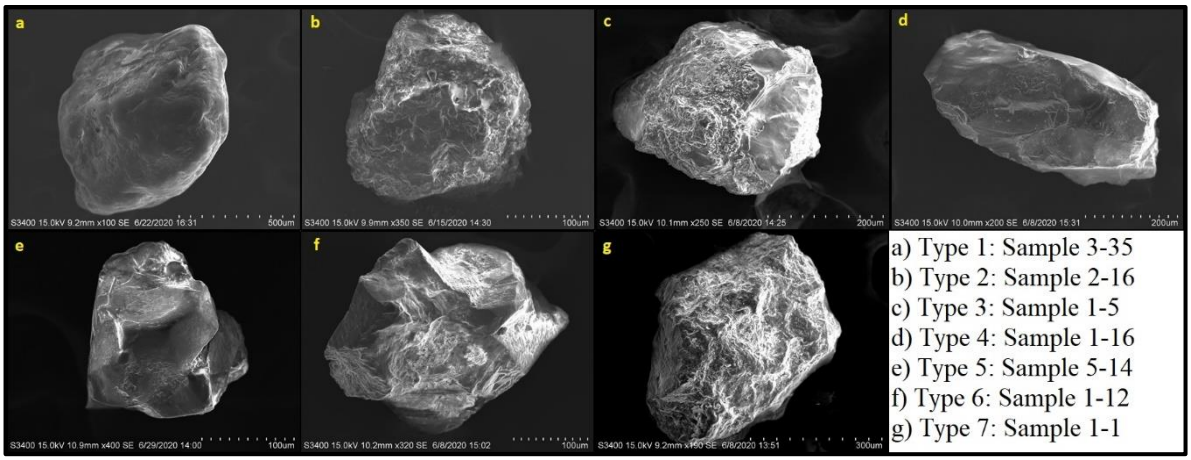

Figure 14: The 7 grain types with images of examples and the corresponding sample name. For example, (a) shows the grain #35 from Sample 3. Grain Type 1 characteristics include rounded/sub-rounded, low relief, little to no silica dissolution, and little to no fractures. It is determined not to be glacially influenced and, therefore, not an IRD type of grain. Grain Type 2 characteristics include rounded/sub-rounded, low/medium relief, some or most silica dissolution, and little to no fractures. Grain Type 3 characteristics include sub-rounded/sub-angular, low/medium relief, some or most silica dissolution, and fractures present. Grain Type 4 characteristics include rounded/sub-rounded, low/medium relief, little to no silica dissolution, and fractures present. Grain Type 5 characteristics include angular/sub-angular, low/medium relief, little to no silica dissolution, and fractures present. Grain Type 6 characteristics include angular/sub-angular, medium/high relief, some or most silica dissolution, and fractures present. Grain Type 7 characteristics include angular/sub-angular, medium/high relief, some or most silica dissolution, little to no fractures.

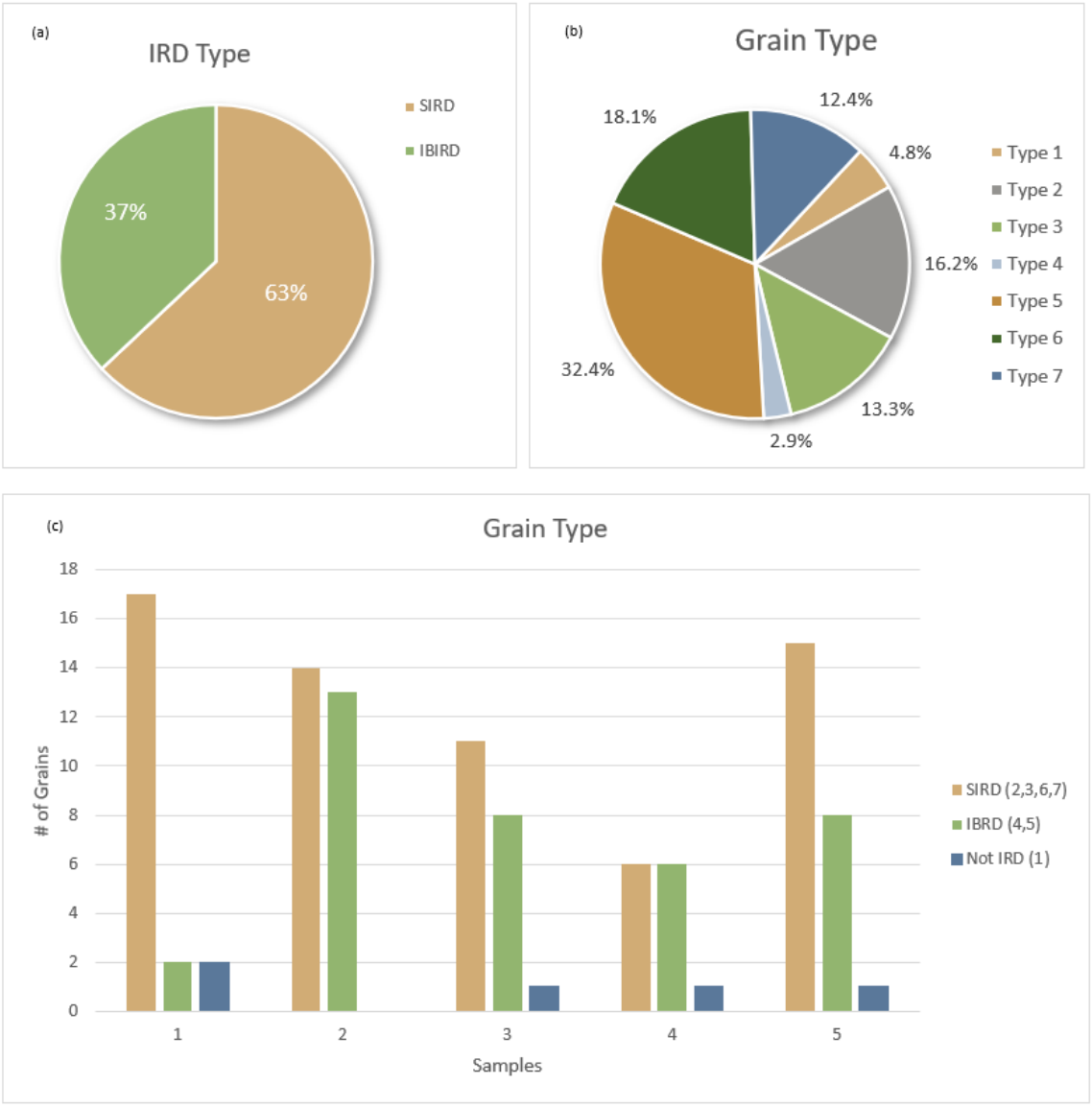

Figure 15: (a) Overall percentage of SIRD and IBRD types in Cores 53R and 54R; (b) Percentage of each grain type in Cores 53R and 54R; (c) The number of grain types for samples 1-5 where SIRD is types 2, 3, 6, and 7, IBRD is types 4 and 5, and not IRD is type 1.

4. DISCUSSION

4.1 Paleoclimate Conditions

4.1.1 Sedimentological Analysis

Grain size distribution from laser particle size analysis is used to infer environmental settings at the time of deposition and provide an overall understanding of ice sheet behavior. There is a fining upward trend in Core 54R where the volume percentage for sand decreases but increases for clay, regardless of IRD input. This suggests that from 33.48 to 33.36 Ma, there is a shallow environment with transgression due to relative sea level rise which allows for fine sediments to deposit. It is difficult to determine a similar trend in Core 53R, specifically in Section 53R-5 (Barker et al., 1988). The pie charts in Figures 7 and 8 display generally consistent grain size distributions with silt as the dominant grain size. However, there is a decreasing trend in the abundance of clay. Therefore, from 33.31 to 33.13 Ma, this may have been an inner shelf environment with relative sea level drop. Ice sheet expansion resulting in crustal subsidence would cause fluctuations of sea level at this site (Houben et al., 2013). Furthermore, a coarsening upwards sequence with increases in flux of IRD indicates ice-sheet expansion and glacial calving occurring near the inner shelf environment (St. John, 2008).

IRD MAR can indicate the degree of ice cover where high values signify an advancing ice sheet with calving and low values signify a lack of ice sheets or ice sheets that have not reached surface waters due to warmer paleoenvironments (Passchier et al., 2011). Assessing uniformity along with IRD MAR is also used to indicate ice sheet behaviors. For example, a high IRD MAR with a low uniformity value represents an

increase in sand percentage because of winnowing caused by currents. Conversely, a high IRD MAR with a high uniformity value represents an increase in sand percentage due to an increase in transportation of IRD. Winnowing is visible at 549.11 mbsf in Core 53R and at 560.63 mbsf in Core 54R. Overall, spikes in uniformity coincide with spikes in IRD MAR such as at 555.24 mbsf in Core 53R and 561.72 mbsf in Core 54R (Figures 11d and 11e). The presence of current sorting during deposition of the fine fraction is supported due to r values consistently greater than 0.5 for the two sortable silt parameters.

The scalar flow of bottom currents was determined where Core 54R has a faster average flow speed than Core 53R but remains mostly constant. Core 53R has a faster maximum flow speed than Core 54R but increases upcore. Since we see that current sorting is involved from the r values, and the scalar flow of bottom currents is increasing, it is possible that the cyclone similar to the Weddell Sea Gyre we see today increased in velocity upcore. The correlation between mean SS and scalar flow of bottom currents related to climatic shifts in glacial periods is complicated and multifaceted, requiring additional assumptions such as water depth and volume fluxes (McCave et al., 2017).

4.1.2 Distribution of IRD

IRD is terrigenous sediment, usually coarse-grained, transported to an aqueous environment by ice. Specifically, IBRD is transported by glaciers and calved by icebergs, so that the sediment has avoided periglacial environments and chemical weathering. Therefore, glacial microtextures are often preserved in IBRD. In addition, SIRD is transported to marine environments, rafted by sea ice, and is subject to increased chemical weathering. Hence, it is common for SIRD to have overprinting of marine signatures due to proximity of periglacial environments (St. John et al., 2014).

In addition to different sedimentological histories, it is also important to distinguish between these two types of IRD since these have unique roles in climate feedbacks. For example, a reduction of sea ice leads to reduced albedo, and insolation of warm ocean temperatures is lost. As a result, there is an increase in atmospheric heat transport from the ocean, thus providing a positive feedback system and reinforcing the initial warming (Serreze et al., 2009). The further melting of glaciers increases eustatic sea level. However, melting of sea ice will not affect sea level (St. John et al., 2014). Additionally, glacial and sea ice have a higher albedo and reflect more solar energy than dark surfaces such as seawater. Consequently, when melting of glacial and sea ice occurs, the Earth's albedo is reduced and surface warming increases since more solar energy is absorbed (Perovich et al., 2002). Other impacts on the Earth system as a result of sea ice melt include increase in moisture in the atmosphere which affects the global distribution of precipitation and an increase in ocean salinity which can alter the global thermohaline circulation (St. John et al., 2014).

It was determined that SIRD resembles Grain Types 2, 3, 6, and 7, specifically where silica dissolution is visible but also where roundness is typical. IBRD resemble Grain Types 4 and 5, specifically where little to no silica dissolution is visible, but also where grains are angular/sub-angular. As shown in Figure 14, Grain Type 1 has an absence of silica dissolution, no fractures present, and is rounded. Therefore, it is not considered to be glacially influenced and is not grouped into an IRD type. It is apparent that based on the variety of surface microtextures and features identified, the quartz grains underwent numerous sedimentary processes and originate from multiple depositional environments. Consequently, it is difficult to establish a trend in microtextures between Cores 53R and

54R. For example, the ratio of the presence versus the absence of silica dissolution is roughly equal for each sample. Although, the presence of silica dissolution is slightly more abundant than the absence of silica dissolution in each sample except for Sample 4 (Figure A.2). In contrast, there is a visible trend seen in the ratio of angular/sub-angular grains to rounded/sub-rounded grains. In this case, the quartz grains from Samples 1-3 of Core 54R are largely more angular/sub-angular than rounded/sub-rounded. In Samples 4 and 5 of Core 53R, the ratio is roughly equal (Figure A.4). Additionally, there is a higher abundance of fractures present for Samples 1-3 of Core 54R than in Samples 4 and 5 of Core 53R (Figure A.3).

Since the quartz grains are largely more angular/sub-angular and have a higher abundance of fractures for Samples 1-3 of Core 54R, it is possible that glacial calving was occurring more frequently in Core 54R between 33.36 and 33.48 Ma, prior to the start of Section 53R-5 at 33.31 Ma. Based on this, I would not expect to see an abundance of silica dissolution in the IRD grains for Samples 1-3 of 54R. However, as stated above, this is not the case and silica dissolution is abundant (Figure A.2). Another feature analyzed is the relief of the grains where high relief is a characteristic of IBRD. High relief is rare in Samples 1, 2, and 3 and absent in Samples 4 and 5. Unfortunately, sometimes it is difficult to discern between high and medium relief. Therefore, I combined high and medium relief grains to compare against the number of low relief grains. This resulted in a higher ratio of high and medium relief grains compared to low relief grains in every sample except Sample 3 which has an equal number of high and low relief grains (Figure A.5). Additionally, in another attempt to identify trends in the stratigraphic distribution of Cores 53R and 54R, I looked for a correlation of four features that pertain to IBRD. This includes high/medium

relief, presence of fractures, angular/sub-angular grains, and absence of silica dissolution. This resulted in a low of 47% in Sample 5 in Core 53R and a high of 73% in Sample 2 of Core 54R of grains displaying the four features for IBRD.

As stated above, there is an overall absence of trends of IRD features and types with depth of the core since SIRD and IBRD are identified in copious amounts for each sample. However, since Samples 1-3 of Core 54R are more angular/sub-angular with a higher abundance of fractures, this may be considered a trend of glacial calving occurring more frequently between 33.36 and 33.48 Ma. Even so, trends may be visible if more samples are analyzed using SEM for Cores 53R and 54R. Regardless, microtextures is not a reliable technique on its own to determine the definite ratio of SIRD to IBRD since often times, SIRD can have overprinting of glacial signatures (St. John et al., 2014). Nevertheless, evidence of glaciation is most clearly distinguished based on its characteristic microtextures.

4.1.3 Chemical Weathering

The general proportions of clay minerals can signify a shift in weathering, i.e., from warming to cooling environments. Strong physical weathering and weak chemical weathering can be identified through abundances of chlorite and illite clay minerals. Also, intensification of chemical weathering in feldspars leads to an increase in kaolinite and smectite (Passchier et al., 2017). In Cores 53R and 54R, clay minerals are predominantly smectite (60% to 100%) with a lesser abundance of illite (5% to 55%), and rare, but still present amounts of chlorite and kaolinite (5% to 30%), as described in the Site Report for site 696 (Figure 16) (Barker et al., 1988). Estimated values of smectite for 53R and 54R

are 35-55% (abundant) and 60-90% (very abundant), respectively. The smectite abundance is estimated to be lower in 53R than in cores below. Chlorite is estimated at 15%-30% (common) and 5-10% (rare), for 53R and 54R, respectively. The chlorite abundance is estimated to be higher in 53R than cores below. Illite is estimated at 35-55% (abundant) and 15-30% (common) for 53R and 54R, respectively. The illite abundance in 53R is greater than cores directly below 54R. Kaolinite values are insignificant in these estimations and are included in chlorite values. Overall, the mineral abundances are mostly consistent with values directly above and below 53R and 54R which signifies a steady weathering regime, although the slight relative increase in illite upcore points to enhanced physical weathering.

Paleoclimate reconstructions of the Antarctic Peninsula display cooling temperatures and a decrease in precipitation rates leading up to the EOT and prior to glaciation (Feakins et al., 2014). This is also consistent with the Prydz Bay region in East Antarctica where CIA values are considered to be glacial (<62) which was first identified at approximately 34.2 Ma (Passchier et al., 2017). This signifies progressive cooling with a drier environment. However, clay mineralogical analyses of the Ross Sea show the first appearances of chlorite and illite which represent cooling and large continental ice sheets occurring at approximately 32.8 Ma (Ehrmann et al., 2005). This suggests that cooling in West Antarctica occurred later than in East Antarctica (Galeotti et al., 2016). In general, at Site 696 the estimations show an overall increase in chlorite and illite than the cores below while estimations of smectite remain mostly constant (Figure 16). Calculating CIA values for 53R and 54R would provide additional insight regarding the specific weathering regime.

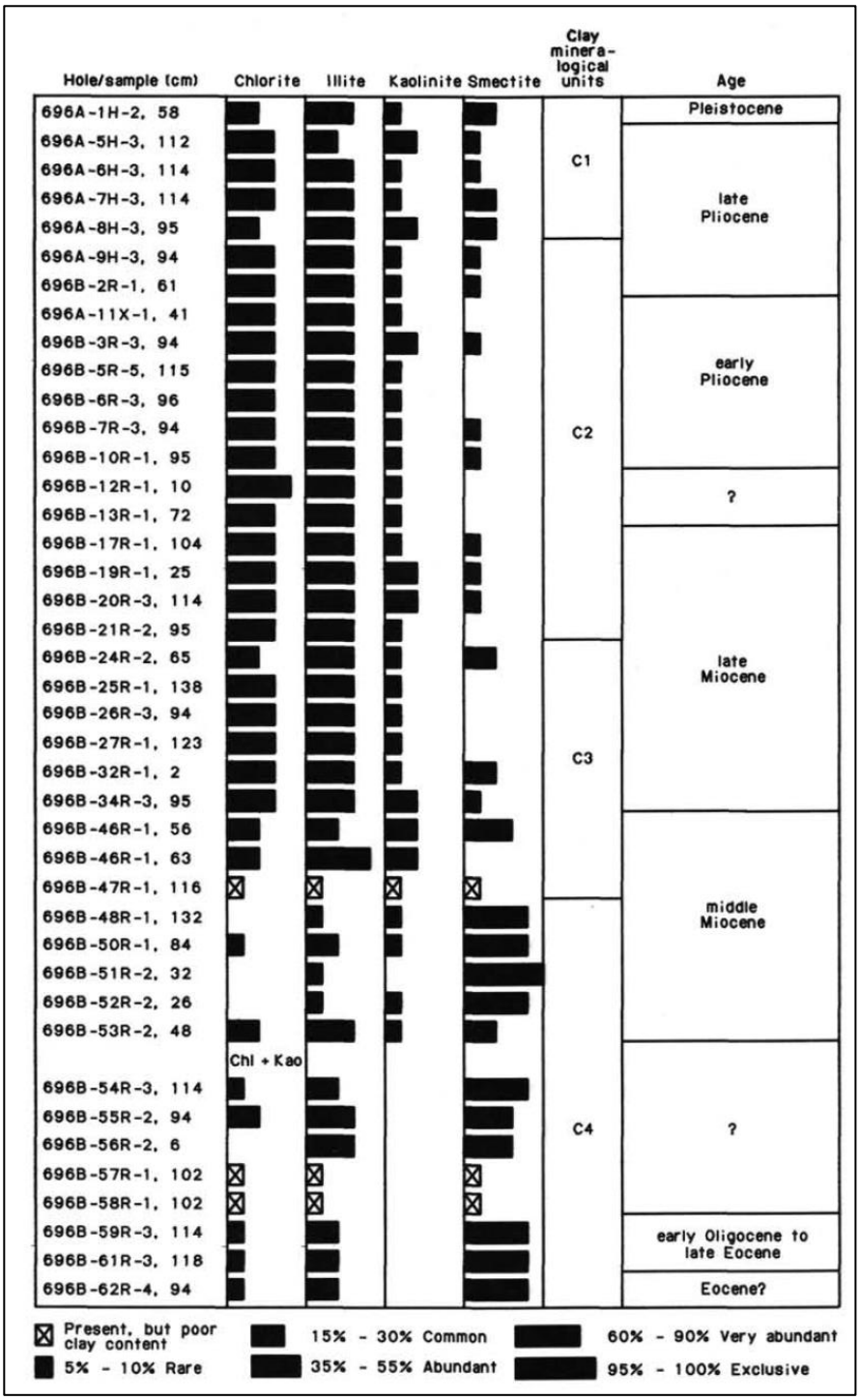

Figure 16: Clay mineralogical estimations for Site 696 (Barker et al., 1988). In Cores 53R and 54R, clay minerals are predominantly smectite (60% to 100%) with a lesser abundance of illite (5% to 55%), and rare, but still present amounts of chlorite and kaolinite (5% to 30%). Estimated values of smectite for 53R and 54R are 35-55% (abundant) and 60-90% (very abundant), respectively. The smectite abundance is estimated to be lower in 53R than in cores below. Chlorite is estimated at 15%-30% (common) and 5-10% (rare), for 53R and 54R, respectively. The chlorite abundance is estimated to be higher in 53R than cores below. Illite is estimated at 35-55% (abundant) and 15-30% (common) for 53R and 54R, respectively. The illite abundance in 53R is greater than cores directly below 54R. Kaolinite values are insignificant in these estimations and are included in chlorite values (Barker et al., 1988).

5. CONCLUSION

The timing of stable, continental-scale ice sheets during the EOT has not been fully ascertained since previous studies show conflicting results. Reconstruction of Antarctica's topography was modeled to show the growth of ice sheets at the EOT in Wilson et al. (2013) where results from the model show formation of the WAIS at 33.8-33.5 Ma alongside expansion of the East Antarctic Ice Sheet. It was suggested that there was considerable glaciation in the inner continent prior to the EOT (Wilson et al., 2013). Carter et al. (2017) analyzed provenance and microtextures of sediments from the South Orkney Microcontinent (SOM) in the Ocean Drilling Program (ODP) Leg 113 Site 696 but Cores 53R and 54R were not part of this study.

This research focuses on grain size and microfeatures of IRD in the stratigraphic record as a proxy for ice sheet advance during the EOT and to determine a more precise timing of continental ice sheets in West Antarctica. Provenance and CIA for sedimentological analysis are also valuable in providing an accurate historical record for the origins of sediments and weathering regimes.

This research suggests that the depositional environment was shallow with transgression occurring with fluctuations in relative sea level due to crustal subsidence from ice sheet expansion. Based on coarsening sequences in bulk density as well as fluxes in IRD, ice sheet expansion and glacial calving is evident during this time in the stratigraphic record. Furthermore, based on the array of microtextures identified in quartz grains, the grains underwent a variety of weathering processes and originated from different depositional environments. Although trends in microfeatures were mostly absent in the stratigraphic record, approximately 60% of the quartz grains are considered to be

SIRD and 35% are IBRD, and 5 are not glacially influenced. This research concludes that IRD is present in the early Oligocene. Although the precise timing of continental-scale glaciation during the EOT is debated, this research supports that ice-sheets were present in West Antarctica with widespread cooling and extensive glaciation in the earliest Oligocene at 33.48 Ma.

It is evident that research on the EOT must continue to fully understand the response of ice sheet dynamics in a cooling period. This will enable us to develop models to predict future conditions of ice sheets and global climate in our current state of global warming. Furthermore, it will provide a greater comprehension to the immediate effects of melting ice sheets, both locally and globally. It is clear there are differing results and contradictory interpretations to the precise timing of extensive glaciation in Antarctica during the EOT. Therefore, high-resolution research needs to continue growing and evolving.

6. REFERENCES

Anderson, J. B., Warny, S., Askin, R. A., Wellner, J. S., Bohaty, S. M., Kirshner, A. E., … Majewski, W. (2011). Progressive Cenozoic cooling and the demise of Antarctica's last refugium. *Proceedings of the National Academy of Sciences of the United States of America*, *108*(28), 11356–11360. https://doi.org/10.1073/pnas.1014885108

Artemieva, I. M., & Thybo, H. (2020). Continent size revisited: Geophysical evidence for West Antarctica as a back-arc system. *Earth-Science Reviews*, *202*(January). https://doi.org/10.1016/j.earscirev.2020.103106

Barker, P. E., Kennett, J. P., et al., 1988. *Proceedings of the Ocean Drilling Program*. *Initial Reports.*, 113: College Station, Texas (Ocean Drilling Program). doi:10.2973/odp.proc.ir.113.1988

Bromwich, D. H., Nicolas, J. P., Monaghan, A. J., Lazzara, M. A., Keller, L. M., Weidner, G. A., & Wilson, A. B. (2013). Central West Antarctica among the most rapidly warming regions on Earth. *Nature Geoscience*, *6*(2), 139–145. https://doi.org/10.1038/ngeo1671

Carter, A., Riley, T. R., Hillenbrand, C. D., & Rittner, M. (2017). Widespread Antarctic glaciation during the Late Eocene. *Earth and Planetary Science Letters*, *458*(January), 49–57. https://doi.org/10.1016/j.epsl.2016.10.045

Coxall, H. K., & Wilson, P. A. (2011). Early Oligocene glaciation and productivity in the eastern equatorial Pacific: Insights into global carbon cycling. *Paleoceanography*, *26*(2), 1–18. https://doi.org/10.1029/2010PA002021

Coxall, H. K., Wilson, P. A., Pälike, H., Lear, C. H., & Backman, J. (2005). Rapid stepwise onset of Antarctic glaciation and deeper calcite compensation in the Pacific Ocean. *Nature*, *433*(7021), 53–57. https://doi.org/10.1038/nature03135

Damiani, D., Giorgetti, G., & Turbanti, I. M. (2006). Clay mineral fluctuations and surface textural analysis of quartz grains in Pliocene-Quaternary marine sediments from Wilkes Land continental rise (East-Antarctica): Paleoenvironmental significance. *Marine Geology*, *226*(3–4), 281–295. https://doi.org/10.1016/j.margeo.2005.11.002

Dunhill, G. (1998). *Comparison of Sea-ice and Glacial-ice Rafted Debris: Grain Size, Surface Features, and Grain Shape*. Menlo Park, California.

Ehrmann, W., Setti, M., & Marinoni, L. (2005). Clay minerals in Cenozoic sediments off Cape Roberts (McMurdo Sound, Antarctica) reveal palaeoclimatic history. *Palaeogeography, Palaeoclimatology, Palaeoecology*, *229*(3), 187–211. https://doi.org/10.1016/j.palaeo.2005.06.022

Feakins, S. J., Warny, S., & DeConto, R. M. (2014). Snapshot of cooling and drying before onset of Antarctic Glaciation. *Earth and Planetary Science Letters*, *404*(August), 154–166. https://doi.org/10.1016/j.epsl.2014.07.032

Flowerdew, M. J., Millar, I., Curtis, M. ., & Fanning, C. M. (2007). Combined U-Pb geochronology and Hf isotope geochemistry of detrital zircons from early Paleozoic sedimentary rocks, Ellsworth-Whitmore Mountains block, Antarctica. *Geological Society of America Bulletin*, *119*(3–4), 275–288.

Galeotti, S., DeConto, R., Naish, T., Stocchi, P., Florindo, F., Pagani, M., & Barrett, P. (2016). Antarctic ice sheet variability across the Eocene-Oligocene boundary climate transition. *Science*, *352*(6281), 76–80. https://doi.org/10.1126/science.aab0669

Hammer, Ø., Harper, D. A. T., & Ryan, P. D. (2001). PAST: Paleontological Statistics Software Package For Education And Data Analysis. *Palaeontologia Electronica*, *4*(1), 1–9.

Holland, P. R., Bracegirdle, T. J., Dutrieux, P., Jenkins, A., & Steig, E. J. (2019). West Antarctic ice loss influenced by internal climate variability and anthropogenic forcing. *Nature Geoscience*, *12*(9), 718–724. https://doi.org/10.1038/s41561-019-0420-9

Houben, A. J. P., Bijl, P. K., Pross, J., Bohaty, S. M., Passchier, S., Stickley, C. E., … Yamane, M. (2013). Reorganization of Southern ocean plankton ecosystem at the onset of antarctic glaciation. *Science*, *340*(6130), 341–344. https://doi.org/10.1126/science.1223646

Jordan, T. A., Riley, T. R., & Siddoway, C. S. (2020). The geological history and evolution of West Antarctica. *Nature Reviews Earth & Environment*, *1*(2), 117–133. https://doi.org/10.1038/s43017-019-0013-6

Katz, M. E., Miller, K. G., Wright, J. D., Wade, B. S., Browning, J. V., Cramer, B. S., & Rosenthal, Y. (2008). Stepwise transition from the Eocene greenhouse to the Oligocene icehouse. *Nature Geoscience*, *1*(5), 329–334. https://doi.org/10.1038/ngeo179

Konert, M., & Vandenberghe, J. (1997). Comparison of laser grain size analysis with pipette and sieve analysis: A solution for the underestimation of the clay fraction. *Sedimentology*, *44*(3), 523–535. https://doi.org/10.1046/j.1365-3091.1997.d01-38.x

Livermore, R., Nankivell, A., Eagles, G., & Morris, P. (2005). Paleogene opening of Drake Passage. *Earth and Planetary Science Letters*, *236*(1–2), 459–470. https://doi.org/10.1016/j.epsl.2005.03.027

López-Quirós, A., Escutia, C., Sánchez-Navas, A., Nieto, F., Garcia-Casco, A., Martín-Algarra, A., … Salabarnada, A. (2019). Glaucony authigenesis, maturity and alteration in the Weddell Sea: An indicator of paleoenvironmental conditions before the onset of Antarctic glaciation. *Scientific Reports*, *9*(1), 13580. https://doi.org/10.1038/s41598-019-50107-1

Malvern Instruments Ltd. (2007). *Malvern Mastersizer 2000: User Manual MAN0384, 1.0*. United Kingdom: Malvern Instruments Ltd.

McCave, I. N., & Andrews, J. T. (2019). Distinguishing current effects in sediments delivered to the ocean by ice. I. Principles, methods and examples. *Quaternary Science Reviews*, *212*(April), 92–107. https://doi.org/10.1016/j.quascirev.2019.03.031

McCave, I. N., Thornalley, D., & Hall, I. (2017). Relation of sortable silt grain-size to deep-sea current speeds: Calibration of the 'Mud Current Meter''.' *Deep Sea Research Part 1: Oceanographic Research Papers*, *127*(September), 1–12. https://doi.org/10.1016/j.dsr.2017.07.003

Pälike, H., Lyle, M. W., Nishi, H., Raffi, I., Ridgwell, A., Gamage, K., … Zeebe, R. E. (2012). A Cenozoic record of the equatorial Pacific carbonate compensation depth. *Nature*, *488*(7413), 609–614. https://doi.org/10.1038/nature11360

Passchier, S. (2011). Linkages between East Antarctic Ice Sheet extent and Southern Ocean temperatures based on a Pliocene high-resolution record of ice-rafted debris off Prydz Bay, East Antarctica. *Paleoceanography*, *26*(4), pA4204. https://doi.org/10.1029/2010PA002061

Passchier, S., Ciarletta, D. J., Henao, V., & Sekkas, V. (2018). Sedimentary processes and facies on a high-latitude passive continental margin, Wilkes Land, East Antarctica End. *Geological Society London Special Publications*, *475*(December), 181–201. https://doi.org/10.1144/SP475.3

Passchier, S., Ciarletta, D. J., Miriagos, T. E., Bijl, P. K., & Bohaty, S. M. (2017). An antarctic stratigraphic record of stepwise ice growth through the eocene-oligocene transition. *Bulletin of the Geological Society of America*, *129*(3–4), 318–330. https://doi.org/10.1130/B31482.1

Perovoch, K., Grenfell, T. C., Light, B., & Hobbs, P. V. (2002). Seasonal evolution of the albedo of multiyear Arctic sea ice. *Journal of Geophysical Research: Oceans*, *107*(C10), SHE 20-1-SHE 20-13. https://doi.org/10.1029/2000JC000438

Powers, M. C. (1953). A new roundness scale for sedimentary particles. *Journal of Sedimentary Research*, *23*(2), 117–119. https://doi.org/10.1306/D4269567-2B26-11D7-8648000102C1865D

Ryan, W. B. F., Carbotte, S. M., Coplan, J., O'Hara, S., Melkonian, A., Arko, R., … Zemsky, R. (2009). Global Multi-Resolution Topography (GMRT) synthesis data set. *Geochem. Geophys. Geosyst.*, *10*(3), 1–9. Retrieved from https://doi.org/10.1029/2008GC002332

Serreze, M. C., Barrett, A., Stroeve, J. C., Kindig, D. N., & Holland, M. M. (2009). The emergence of surface-based Arctic amplification. *The Cryosphere Discussions*, *3*(1), 601–622. https://doi.org/10.5194/tc-3-11-2009

Sperazza, M., Moore, J. N., & Hendrix, M. S. (2004). High-resolution particle size analysis of naturally occurring very fine-grained sediment through laser diffractometry. *Journal of Sedimentary Research*, *74*(5), 736–743. https://doi.org/10.1306/031104740736%0A

St John, K., Passchier, S., Tantillo, B., Darby, D., & Kearns, L. (2014). Microfeatures of modern sea-ice-rafted sediment and implications for paleo-sea-ice reconstructions. *Annals of Glaciology*, *56*(69), 83–93. https://doi.org/10.3189/2015AoG69A586

St. John, K. (2008). Cenozoic ice-rafting history of the central Arctic Ocean: Terrigenous sands on the Lomonosov Ridge. *Paleoceanography*, *23*(1), 1–12. https://doi.org/10.1029/2007PA001483

Tegzes, A. D., Jansen, E., & Telford, R. J. (2015). Which is the better proxy for paleo-current strength: Sortable-silt mean size (mean SS) or sortable-silt mean grain diameter (d_{ss})? A case study from the Nordic Seas. *Geochemistry, Geophysics, Geosystems*, *16*(1), 267–300. https://doi.org/10.1002/2014GC005684.Key

Wentworth, C. K. (1922). A Scale of Grade and Class Terms for Clastic Sediments. *The Journal of Geology*, *30*(5), 377–392. https://doi.org/10.1086/622910

Whitehouse, P. L., Gomez, N., King, M. A., & Wiens, D. A. (2019). Solid Earth change and the evolution of the Antarctic Ice Sheet. *Nature Communications*, *10*(1), 1–14. https://doi.org/10.1038/s41467-018-08068-y

Wilson, D. S., Pollard, D., Deconto, R. M., Jamieson, S. S. R., & Luyendyk, B. P. (2013). Initiation of the West Antarctic Ice Sheet and estimates of total Antarctic ice volume in the earliest Oligocene. *Geophysical Research Letters*, *40*(16), 4305–4309. https://doi.org/10.1002/grl.50797

Zachos, J., Pagani, M., Sloan, L., Thomas, E., & Billups, K. (2001). Cenozoic Climate: From Greenhouse to Icehouse. *Science Mag*, *292*(April), 686–693.

7. APPENDIX

Sample Name
54R-3-68-71
54R-3-89-92
54R-3-98-101
54R-3-126-129
54R-4-31-34

Table A.1: Samples which were diluted during laser particle size analysis due to large amounts of sediments in the solution.

Sample Name	Obscuration
53R-1-30-33 - Average	4.12
53R-2-15-18 - Average	4.67
53R-2-111-114 – Average*	3.83
53R-3-13-16 – Average*	3.7
53R-3-42-45 – Average**	3.3
53R-3-42-45 – Average**	3.84
53R-3-86-89 - Average	5.72
53R-3-96-99 – Average*	2.98
53R-3-115-118 - Average	5.22
53R-4-101-104 – Average**	2.98
53R-4-101-104 – Average**	5.36
53R-4-113-116 – Average*	3.26
53R-5-44-47 - Average	5.2
53R-5-72-75 - Average	5.59

Table A.2: Samples excluded from grain size distribution analysis due to low obscuration (< 6%) and are not displayed in figures. *Samples with 1 asterisk were analyzed in the laser particle sizer two times, and only results from the second run are included in analyses and figures. **Samples with 2 asterisks were analyzed in the laser particle sizer two times, and both runs received obscuration values too low for analyses; neither run is included in analyses and figures.

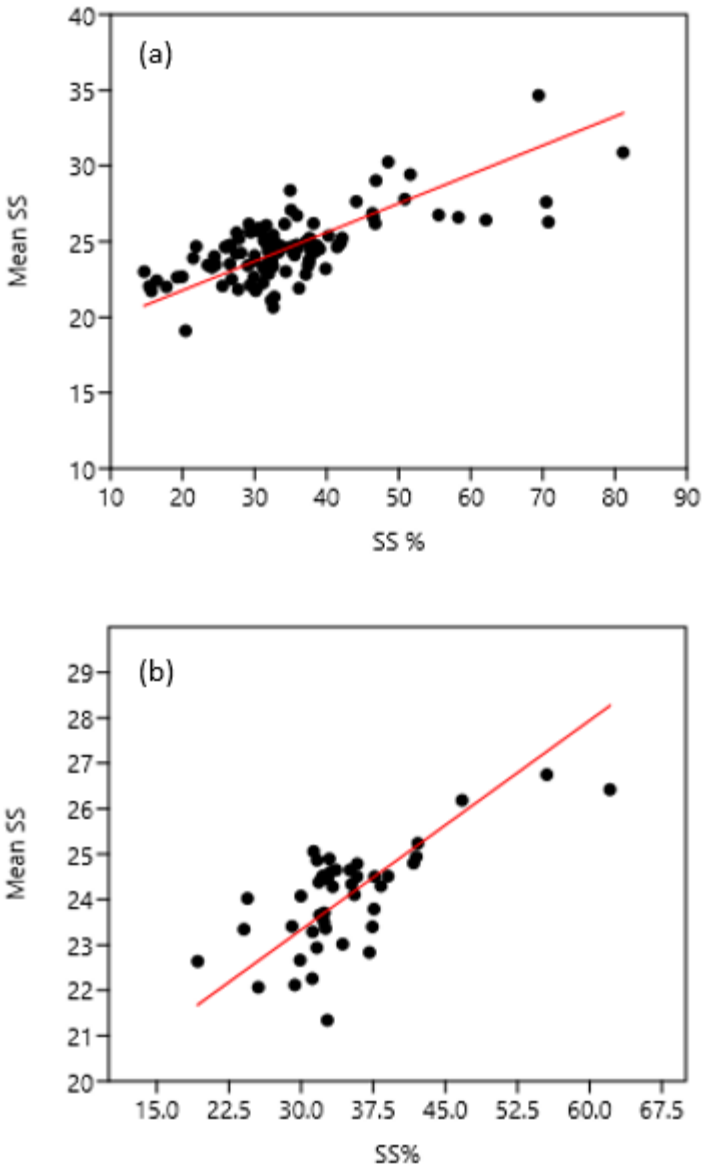

Figure A.1: Bivariate plot of Sortable Silt (SS) % versus Mean SS: (a) 53R, where r = 0.73 and equation of the line is, $y = 0.19x + 18.26$; (b) 54R, where r = 0.69 and equation of the line is, $y = 0.15x + 18.72$. R values greater than 0.5 indicates current sorting is involved in the sedimentation process.

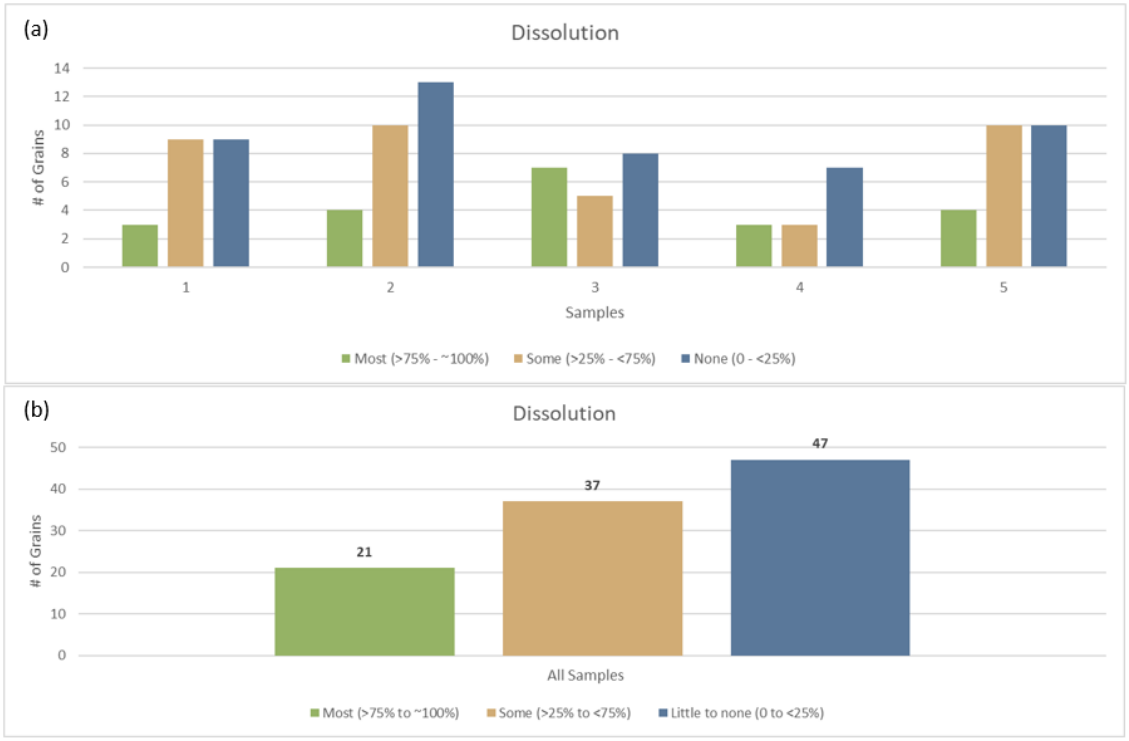

Figure A.2: Number of grains categorized by amount of dissolution: (a) for SEM samples 1-5; (b) total for all samples.

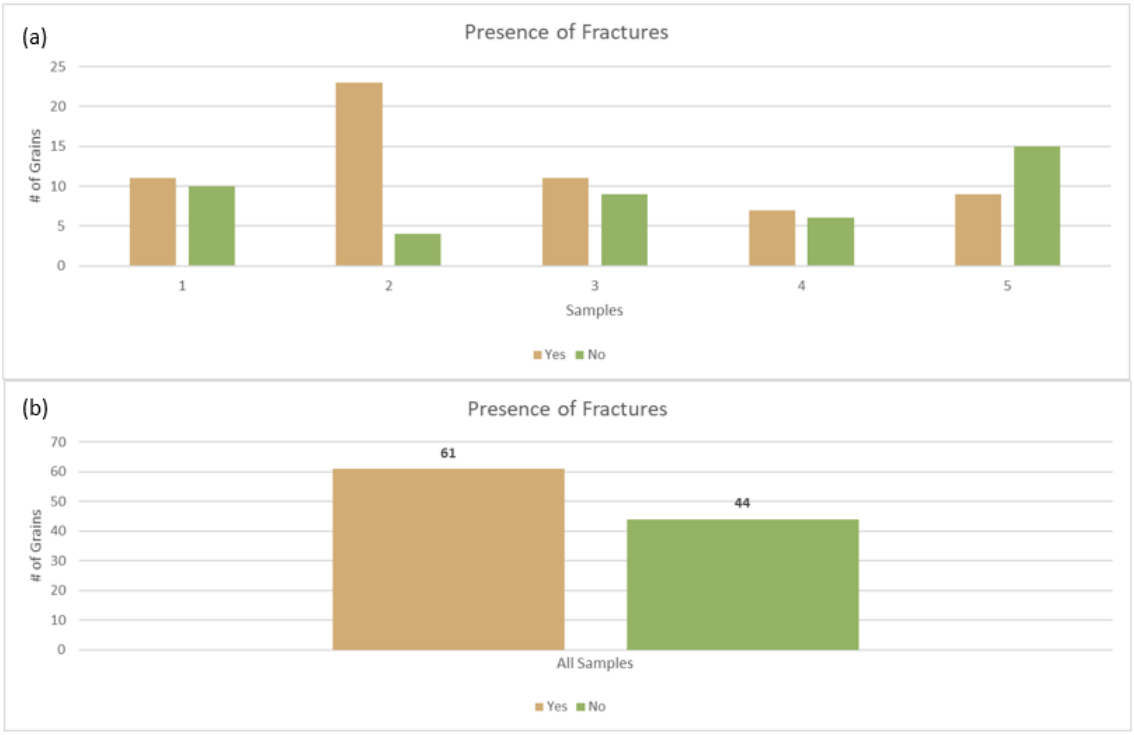

Figure A.3: Number of grains categorized by presence of fractures: (a) for SEM samples 1-5; (b) total for all samples.

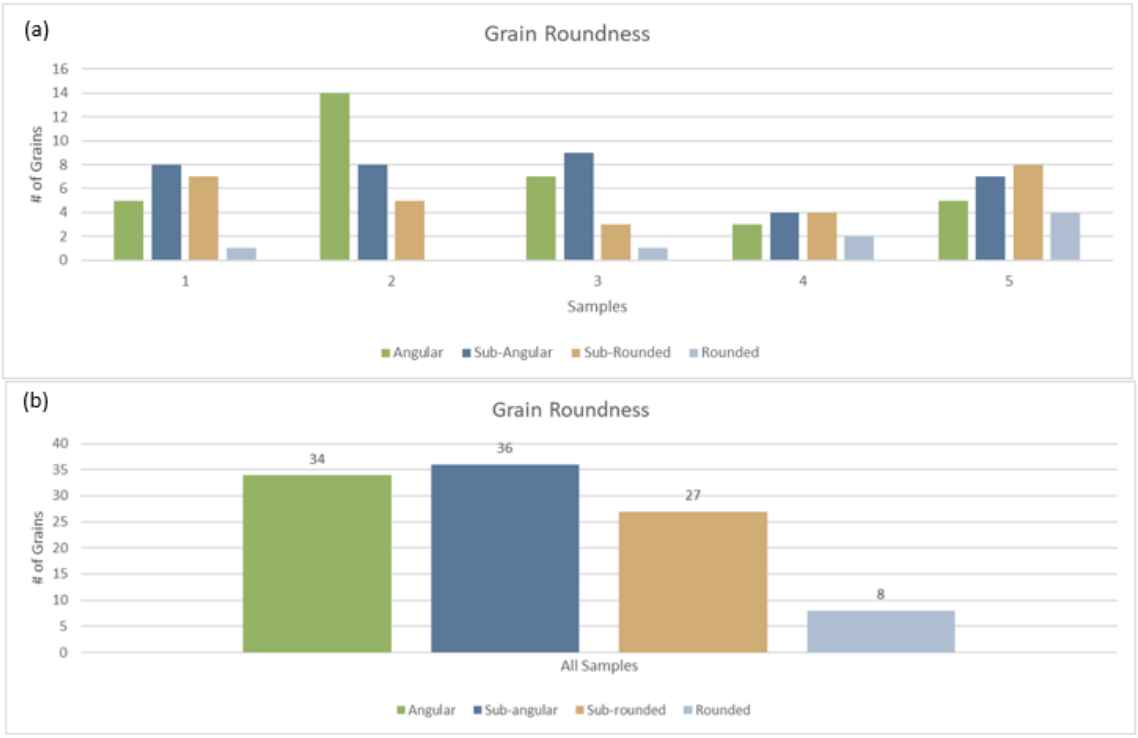

Figure A.4: Number of grains categorized by grain roundness: (a) for SEM samples 1-5; (b) total for all samples.

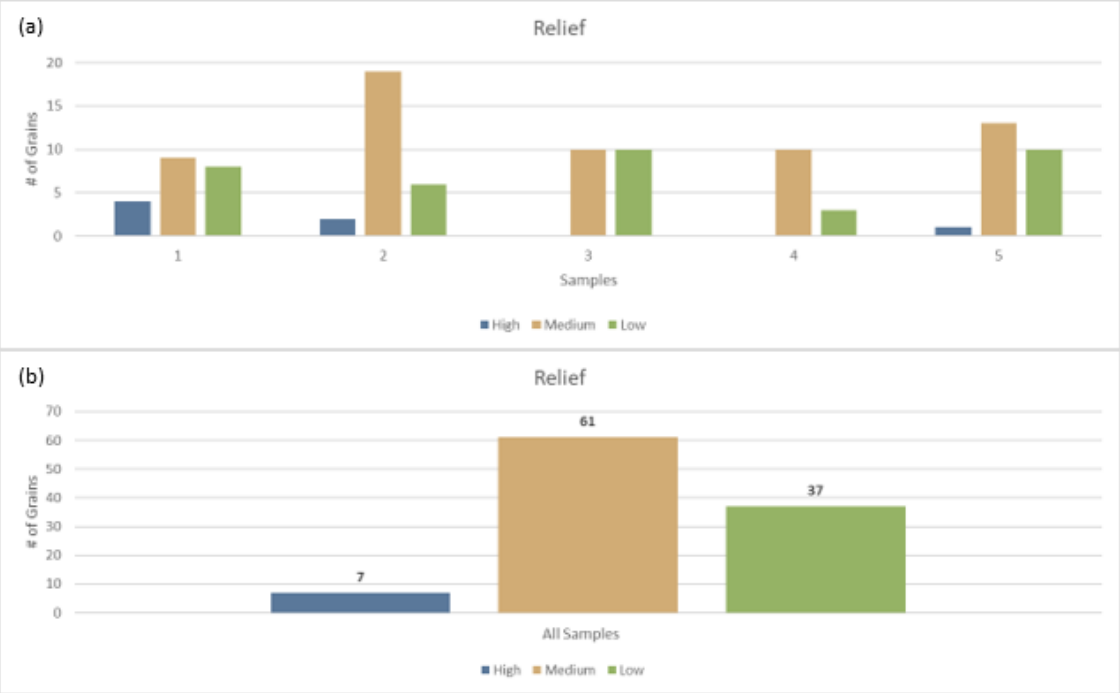

Figure A.5: Number of grains categorized by grain relief: (a) for SEM samples 1-5; (b) total for all samples.

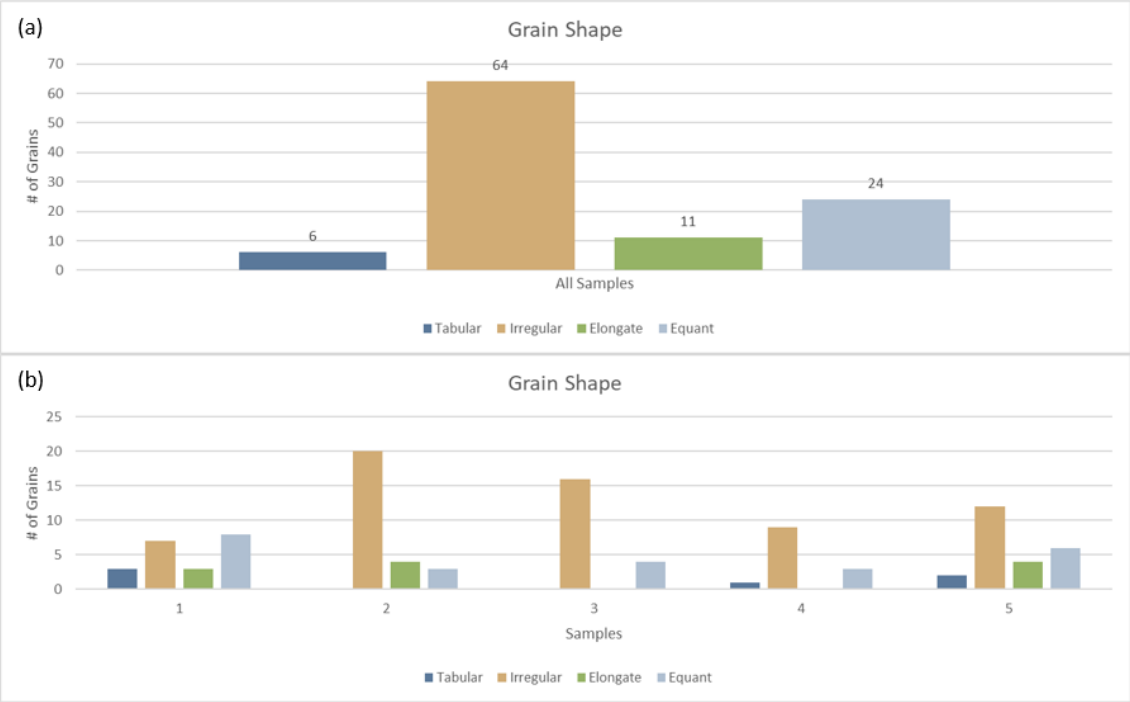

Figure A.6: Number of grains categorized by grain shape: (a) for SEM samples 1-5; (b) total for all samples.